

Convergence Properties of Finite-Difference Hydrodynamics Schemes in the Presence of Shocks

Paul A. Kimoto

Department of Physics, Cornell University, Ithaca, NY 14853

and

David F. Chernoff

Department of Astronomy, Cornell University, Ithaca, NY 14853

ABSTRACT

We investigate asymptotic convergence in the $\Delta x \rightarrow 0$ limit as a tool for determining whether numerical computations involving shocks are accurate. We use one-dimensional operator-split finite-difference schemes for hydrodynamics with a von Neumann artificial viscosity. An internal-energy scheme converges to demonstrably wrong solutions. We associate this failure with the presence of discontinuities in the limiting solution. Our extension of the Lax-Wendroff theorem guarantees that certain conservative, operator-split schemes converge to the correct continuum solution. For such a total-energy scheme applied to the formation of a single shock, convergence of a Cauchy error approaches the expected rate slowly. We relate this slowness to the effect of varying diffusion, due to varying linear artificial-viscous length, on small-amplitude waves. In an appendix we discuss the scaling of shock-transition regions with viscous lengths, and exhibit several difficulties for attempts to make extrapolations.

1. Introduction

Finite-difference hydrodynamics schemes find widespread use in astrophysical applications, where they are often parts of computations that involve other significant physical processes, such as external heating and radiative cooling. In this paper we consider numerical methods for establishing the accuracy of a calculation in the presence of shocks. Our primary tool is testing for convergence. We require that calculations not merely converge, but converge at or near the expected asymptotic rate. This accuracy criterion should readily lend itself to automated refinement methods in which grids are made denser only when and where required for accuracy.

For our investigations we use the one-dimensional Euler equations modified by the inclusion of an explicit artificial viscosity. The numerical schemes are operator-split and explicit. We describe two schemes: a *non-conservative* form that uses the internal-energy density as a primary

variable, as is common in astrophysical calculations (e.g., Norman & Winkler 1986, Stone & Norman 1992, and Hawley, Smarr & Wilson 1984), and a similar *conservative* form that instead uses the total-energy density as a primary variable.

In this paper we investigate the performance of these schemes in simple test problems with shocks. After outlining the numerical methods in section 2, we show in section 3 that the non-conservative internal-energy scheme converges to incorrect solutions when shocks develop. This failure occurs when artificial-viscous lengths and gridsize are decreased proportionally, as is the usual practice. When viscous lengths are held fixed as the gridsize tends to zero, however, the scheme converges to a correct solution (albeit to a different physical problem). Section 4 discusses the performance of both schemes in a shock-tube problem. We show explicitly that the internal-energy scheme (for a particular choice of viscous lengths) converges toward a solution with shock speed too low by approximately 0.2%. The other, conservative difference scheme converges toward the correct solution even in the presence of the shock. (We show in Appendix A that its correct behavior is a consequence of the Lax-Wendroff theorem [Lax & Wendroff 1960], which we extend to operator-split schemes.)

Then in section 5 we examine rates of convergence for the conservative scheme. We show that the presence of linear artificial viscosity (proportional to $\partial v/\partial x$) introduces a substantial amount of diffusion. In sequences in which the artificial viscosity vanishes with the gridsize, the variation in diffusion has an observable effect on convergence rates for small-amplitude waves. Finally, we consider a wall-shock problem, which also contains such small-amplitude waves. We consider two kinds of sequences: (1) sequences in which the artificial viscosity enters as a constant term, and (2) sequences in which it varies with the gridsize. Holding the artificial-viscous lengths fixed leads quite readily to small changes and the expected convergence rate. In contrast, in the sequences where the viscosity vanishes with the gridsize, we observe that the convergence rate tends only slowly toward the rate expected. The effect of linear artificial viscosity on post-shock sound waves contributes substantially to this slowness.

Attempts to extrapolate solutions with different viscous lengths must cope with the variation in the widths of transitions that represent shocks. These widths closely scale with the artificial-viscous lengths, but small deviations from exact scaling behavior may pose considerable barriers to extrapolation algorithms. These deviations from scaling are the main subject of Appendix C.

2. Numerical Methods

We refer to our two finite-difference schemes as “internal-energy” and “total-energy,” after the underlying differential equations that they represent. We consider the one-dimensional Euler equations, written in the form

$$\frac{\partial \rho}{\partial t} = -\frac{\partial m}{\partial x} \tag{1}$$

$$\frac{\partial m}{\partial t} = -\frac{\partial}{\partial x} \left[\frac{m^2}{\rho} + P \right] \quad (2)$$

$$\frac{\partial e_{int}}{\partial t} = -\left(\frac{\partial}{\partial x} \left[\frac{e_{int} m}{\rho} \right] + P \frac{\partial m}{\partial x} \frac{1}{\rho} \right) \quad (3)$$

$$\frac{\partial e_{tot}}{\partial t} = -\frac{\partial}{\partial x} \left[(e_{tot} + P) \frac{m}{\rho} \right], \quad (4)$$

where $m = \rho v$ is the momentum density (here per length); e_{int} , the *internal* energy density; e_{tot} , the *total* energy density, and P , the pressure. The equation of state is given by the ideal gas law; generally we take $\gamma = 5/3$. Equations (3) and (4) are alternative expressions of the conservation of energy. In the internal-energy scheme, we apply equation (3); in the total-energy scheme, equation (4).

Since we want to capture shocks automatically and so avoid the computational difficulties of shock tracking, we use an explicit artificial viscosity to generate the entropy necessary for shocks. Following Norman and Winkler (1986), to the physical pressure P we add the term

$$Q = \rho \frac{\partial v}{\partial x} \left[-L_1 c + L_2^2 \min \left(\frac{\partial v}{\partial x}, 0 \right) \right], \quad (5)$$

where c is the adiabatic sound speed. The constants L_1 and L_2 are viscous lengths for linear and quadratic artificial-viscosity terms, and parametrize their strengths. Typically the artificial viscosity smears shock transitions over a region whose size is comparable to the viscous lengths. Conventionally the viscous lengths L_1 and L_2 are chosen to be a small multiple of the gridsize Δx ; we adopt this approach for our initial investigations.

For a finite-difference representation of the equations of motion, we employ an operator-split scheme similar to the internal-energy scheme developed by Norman and Winkler (Norman & Winkler 1986, Stone & Norman 1992). They use a staggered spatial grid, defining scalar and vector quantities at different gridpoints; whereas our grid is unstaggered.

The operator splitting proceeds as follows: for the parts of the equations (1–4) that represent advection,

$$\frac{\partial \psi}{\partial t} = -\frac{\partial [v\psi]}{\partial x}, \quad (6)$$

we use the monotonic advection scheme of van Leer (1977). The rest of the terms are treated in three further substeps: pressure acceleration, artificial viscosity, and compressional heating. In each full timestep, we account first for each of these three terms (in the order specified), and then for the advection terms. Each substep generates new values of the physical variables, which then are used in the update for the next substep.

Explicitly, then, the finite-difference equations take this form: first we represent the pressure-acceleration term by

$$m_j \mapsto m_j - \frac{\Delta t}{2\Delta x} (P_{j+1} - P_{j-1}). \quad (7)$$

To incorporate the artificial-viscosity terms we next use

$$m_j \mapsto m_j - \frac{\Delta t}{2\Delta x} (Q_{j+1} - Q_{j-1}) \quad (8)$$

$$(e_{int})_j \mapsto (e_{int})_j - \frac{\Delta t}{2\Delta x} Q_j (v_{j+1} - v_{j-1}) \quad (9)$$

$$(e_{tot})_j \mapsto (e_{tot})_j - \frac{\Delta t}{2\Delta x} (Q_{j+1}v_{j+1} - Q_{j-1}v_{j-1}), \quad (10)$$

where values of the momentum density—updated by pressure acceleration—enter into the right-hand sides through $v_j = m_j/\rho_j$ and $Q_j = \rho_j(\partial v/\partial x)_j[-L_1c_j + L_2^2 \min(0, (\partial v/\partial x)_j)]$. For the gradient term, we take $(\partial v/\partial x)_j = (v_{j+1} - v_{j-1})/2\Delta x$. Then, in the compressional-heating substep, the energy density is changed by

$$(e_{int})_j \mapsto (e_{int})_j - \frac{\Delta t}{2\Delta x} (e_{int})_j (v_{j+1} - v_{j-1}) \quad (11)$$

$$(e_{tot})_j \mapsto (e_{tot})_j - \frac{\Delta t}{2\Delta x} [(e_{tot})_{j+1}v_{j+1} - (e_{tot})_{j-1}v_{j-1}], \quad (12)$$

where once again the latest values of $(e_{int})_j$, $(e_{tot})_j$, and m_j enter the right-hand sides.

The resulting values of the physical quantities enter the advection substep. The van Leer procedure has the flux-conserving form

$$\psi_j \mapsto \psi_j - \frac{\Delta t}{\Delta x} (\mathcal{F}_{j+1/2} - \mathcal{F}_{j-1/2}). \quad (13)$$

The fluxes $\mathcal{F}_{j+1/2}$ are calculated in the upwind fashion

$$\mathcal{F}_{j+1/2} = \begin{cases} v_{j+1/2} \left[\psi_j - \frac{1}{2} \left(v_{j+1/2} \Delta t / \Delta x - 1 \right) \nabla \psi_{j+1} \right], & \text{if } v_{j+1/2} \geq 0, \\ v_{j+1/2} \left[\psi_{j+1} - \frac{1}{2} \left(v_{j+1/2} \Delta t / \Delta x + 1 \right) \nabla \psi_{j+1} \right], & \text{if } v_{j+1/2} < 0, \end{cases} \quad (14)$$

where $v_{j+1/2} = (v_{j+1} + v_j)/2$, and (as always) $v_j = m_j/\rho_j$. This advection scheme's monotonicity arises from van Leer's definition of the gradient-like term

$$\nabla \psi_j = \begin{cases} 2\delta\psi_{j+1/2}\delta\psi_{j-1/2}/(\psi_{j+1} - \psi_{j-1}) & \text{if } \delta\psi_{j+1/2}\delta\psi_{j-1/2} > 0, \\ 0 & \text{otherwise,} \end{cases} \quad (15)$$

where $\delta\psi_{j+1/2} = \psi_{j+1} - \psi_j$. The spatial accuracy of the van Leer procedure is second-order, except at extrema, where the accuracy must be reduced to first order to guarantee monotonicity. After the advection substep, the update through the timestep Δt is complete.

In regions where the continuum solution is smooth, such difference schemes are consistent with the differential equations (Sod 1985). When discontinuities are present, however, it is not immediately obvious that truncation errors should vanish in the $\Delta x, \Delta t \rightarrow 0$ limit. If we regard truncation errors as products of these small quantities and derivatives of the solution, then clearly it is possible that the truncation errors may remain finite even in the small-gridsize, small-timestep limit.

Lax and Wendroff (1960) proved that single-step *conservative* difference schemes, if stable and convergent, converge to weak solutions of the corresponding systems of conservation laws. This theorem can be directly extended to include operator-split, multi-step conservative schemes as well (see Appendix A). We know of no such theorem or extension for non-conservative schemes, however. Below we present results that show that some non-conservative schemes (namely, our internal-energy type) do *not* converge to weak solutions of conservation laws.

The operator-splitting method limits the overall time accuracy to first order, and the spatial accuracy of the substeps is (almost everywhere) second order. For smooth flows, then, asymptotically the error per step is $O((\Delta t)^2, \Delta t(\Delta x)^2)$.

In general, the need for numerical stability requires constraints on the timestep Δt (Richtmyer & Morton 1967). We impose two constraints. First, the timestep must everywhere satisfy the Courant-Friedrichs-Lewy condition,

$$\Delta t \leq \frac{\Delta x}{|v| + c}. \quad (16)$$

Second, since the artificial viscosity takes the form of diffusion, we enforce a “diffusion-limiting” condition

$$\Delta t \leq \frac{(\Delta x)^2}{L_1 c - 2L_2^2 \min(\partial v / \partial x, 0)}. \quad (17)$$

To ensure these conditions, before making each update we choose the timestep to be

$$\Delta t = \min_{grid} \left[\frac{C\Delta x}{|v| + c}, \frac{D(\Delta x)^2}{L_1 c - 2L_2^2 \min(\partial v / \partial x, 0)} \right], \quad (18)$$

where $C < 1$ and $D < 1$ are safety factors. All of the calculations shown in this paper use $C = D = 0.9$.

Despite these stability constraints, we have found that our total-energy scheme is *unstable* in the limit $\Delta x \rightarrow 0$ when $L_1/\Delta x = \text{constant}$. In our experience, any given unstable calculation may be stabilized by increasing the linear artificial viscous length L_1 . However, *we discourage the use of the total-energy scheme for convergence studies*. Imposing a diffusion-limiting condition (17) means that increasing the artificial viscosity forces smaller timesteps and greater computational expense. We use the scheme in the context of this paper to emphasize that our conclusions regarding the internal-energy scheme are based on that scheme’s non-conservative nature.

In the calculations that we show in this paper, we observe no indications of instability. Further, we have duplicated most of the total-energy calculations with the (likewise conservative) classic Lax-Wendroff scheme (Lax & Wendroff 1960) in two-step form (Richtmyer & Morton 1967). (Some Lax-Wendroff calculations required reduced timesteps for stability, achieved by using a smaller safety factor D .) These verify that our results regarding convergence in the presence of linear artificial viscosity depend on the viscosity, not on the underlying numerical scheme.

3. Nonlinear Sound Wave

Since the internal-energy equation (3) is not in the form of a conservation law, finite-difference schemes based on it do not conserve total energy exactly. Hence, one test of its results is to compare the calculated total energy with the total energy in the initial conditions. Under some conditions this scheme produces incorrect results.

For the first test problem we consider a steepening wave. The initial conditions superpose a large-amplitude wave on a flat background:

$$\begin{aligned} v(x) &= \delta(x) \\ P(x) &= 3/5 + \delta(x) \\ \rho(x) &= 1 + \delta(x), \end{aligned} \tag{19}$$

where

$$\delta(x) = \begin{cases} \delta_0 e^{-[(x-x_0)/\Delta]^2 - [(x-x_0)/\Delta]^4}, & \text{if } |x - x_0| < 2\Delta \\ 0, & \text{otherwise.} \end{cases} \tag{20}$$

For the amplitude we take $\delta_0 = 0.2$; and for the width parameter, $\Delta = 100/13$. In the small-amplitude limit of the inviscid equations of motion, this waveform is a purely right-moving wave. Because of non-linear effects, it steepens and forms a shock on its leading edge. (The grid is large enough that waves from the perturbation do not reach the edges; hence no energy flows in or out the computational volume.) The viscous parameters are $L_1/\Delta x = 1/2$ and $L_2/\Delta x = 1$. We refine the gridsize Δx and compare the results.

Figure 1 illustrates the behavior of the total-energy error ΔE_{total} at various times as a function of gridsize Δx . At early times ($t \leq 20$) the error decreases proportionally to Δx , as anticipated for this first-order accurate scheme. At late times ($t \geq 28$), however, at small values of Δx the energy error tends toward *non-zero* values. For these cases, increasing resolution leads not to greater accuracy, but rather toward some incorrect solution. The internal-energy scheme cannot be performing correctly at late times.

The shock forms at $t = 23 \pm 0.5$, estimated as follows. We repeat the calculations beginning with the same initial conditions but without artificial viscosity. To forestall the onset of numerical instabilities that develop in the absence of linear artificial viscosity, the timestep safety factor C is reduced to 0.4. We use the characteristics moving to the right from each gridpoint at the speed $v + c$ to find the time of first crossing, which corresponds to shock formation. Close examination of the $t = 24$ curve in Figure 1 suggests that it may deviate from the well-behaved curves for $t \leq 20$. Once the shock forms, the non-vanishing energy error becomes increasingly apparent. This experiment strongly suggests that the internal-energy scheme fails when the flow contains a shock.

Before discussing this failure further, we introduce another measure of errors in computed

solutions. Define the Cauchy error for a solution computed with gridsize Δx by

$$\epsilon_{\Delta x}[\psi] = \int_{grid} \left| \psi_{\Delta x}(x, T) - \psi_{\Delta x/2}(x, T) \right| dx, \quad (21)$$

where $\psi_{\Delta x}(x, T)$ is some physical variable (at position x and time T) as computed with gridsize Δx . When the numerical calculations converge to the solution of the continuum system, this error measure should behave as $O((\Delta x)^\alpha)$, where α gives the leading-order behavior of the error. For smooth flows, α is simply the order of accuracy of the scheme. When discontinuities are present, however, α depends also on the changes in the computed transition widths ℓ , which should be on the order of the viscous lengths L_1 and L_2 . (We discuss this issue further in Appendix C.) If the jump across the transition is $\Delta\psi$, then (on dimensional grounds alone) the shock should contribute $\ell\Delta\psi$ (up to numerical constants) to the Cauchy error. When the viscous lengths L_1 and L_2 are taken to be proportional to the gridsize Δx , the contribution to the Cauchy error should also behave as $O(\Delta x)$. (Note, however, that this is a norm-dependent statement. For example, in the commonly used \mathcal{L}_2 norm the error at shock transitions should behave as $O((\Delta x)^{1/2})$.) When computations are sufficiently well-resolved so that solutions converge as expected—that is, $\epsilon[\psi] \propto (\Delta x)^\alpha$, where α has its expected asymptotic value—then they can be regarded as quite close to the $\Delta x \rightarrow 0$ result (Finn & Hawley 1989). Note, however, that the Cauchy error exploits *no* knowledge of the exact continuum solution. In practice one often assumes that convergence at the expected rate implies convergence to the correct solution.

Figure 2 shows that the Cauchy error measures for all three densities (ρ , m , and e_{int}) decrease linearly with decreasing gridsize Δx . This shows that convergence of the Cauchy error alone does *not* imply correct behavior of the numerical scheme. (Since the Cauchy errors for all three quantities behave similarly, in the rest of this paper we illustrate Cauchy errors for the momentum density only.)

Aside from the total-energy error, we have no indications that the internal-energy scheme behaves incorrectly. No numerical instabilities appear, and the performance at pre-shock times is exactly as anticipated. The error itself is relatively small—at $t = 40$ the error in total energy approaches approximately 0.4% of the initial energy in the wave—and has likely gone unnoticed by many users of internal-energy schemes. Since the scheme appears stable and convergent, this finite error clearly shows that non-conservative schemes need not converge to solutions of the conservation laws when discontinuities are present.

Motivated by this hypothesis, we make the following modification: Instead of scaling the viscous lengths L_1 and L_2 with the gridsize Δx , so that $L_1/\Delta x$, $L_2/\Delta x = \text{constants}$, we treat the viscous lengths themselves as constants. This approach changes the differential equations being solved. Viscous effects remain finite even as the gridsize Δx vanishes, and so shocks are replaced by smooth transitions with finite width. With this change, the internal-energy scheme behaves properly at all times. We expect errors proportional to $(\Delta x)^2$, since the scheme’s first-order error is entirely temporal (i.e., $O(\Delta t)$, not $O(\Delta x)$), and, by the diffusion-limiting condition (17), for

sufficiently small Δx the timestep Δt is proportional to $(\Delta x)^2$.

We repeat the steepening-wave problem, now choosing $L_1 = 1/4$ and $L_2 = 1/2$. In Figure 3 we see that, for sufficiently small gridsize Δx , the total-energy error ΔE_{total} tends toward zero as $O(\Delta x)^2$ at all times. Figure 4 shows that the Cauchy error $\epsilon[m]$ also decreases as $O(\Delta x)^2$ at all times. The magnitudes of these errors are much smaller than their counterparts (at the same gridsize Δx) from the previous ($L_1/\Delta x, L_2/\Delta x = \text{constants}$) calculations. This suggests that these finite-gridsize results are quite close to the solutions of the (finite-viscosity) continuum system. Equivalently, it suggests that the Cauchy errors measured in the previous calculations are dominated by the change in viscous lengths L_1 and L_2 , not by effects of the non-zero gridsize.

Although the preceding discussion has focussed on the failure of a particular internal-energy scheme with particular computational parameters, the phenomenon is more general. We have varied the size of the timestep safety factors C and D and the strengths of the viscous parameters $L_1/\Delta x$ and $L_2/\Delta x$ (including setting $L_2 = 0$) with no improvement in results. Further, we have implemented versions with Norman and Winkler’s staggered grid, as well as several other modifications to the difference equations (Norman & Winkler 1986, Stone & Norman 1992), also without improvements in results. (Appendix B details the modifications we have tested.)

It is possible that the scheme may converge toward the inviscid solution if we choose to vary the gridsize Δx and viscous lengths L_1 and L_2 such that $\Delta x, L_1, L_2 \rightarrow 0$ but $L_1/\Delta x, L_2/\Delta x \rightarrow \infty$. In this situation the width of the shock representation should decrease with increasing resolution, but the number of gridpoints in the representation should increase. We do not investigate the behavior of the scheme using this procedure. The slowly decreasing values of L_1 and L_2 impose penalties on computational efficiency [via the diffusion-limiting timestep condition (17)], and it is unclear whether convergence toward a physically reasonable solution can be readily observed without choosing the viscous lengths to be nearly constants.

To summarize, when the flow contains shocks (and the limiting equations are inviscid), the internal-energy scheme converges toward a solution that is demonstrably wrong. This failure arises because the solution contains discontinuities and the difference scheme is non-conservative. We can recover acceptable behavior by changing the equations so that the limiting solution does not contain discontinuities. In the next section we study another test problem in which the internal-energy scheme demonstrably fails, and also show that the total-energy scheme succeeds.

4. Shock Tube

Because we associate the failures of the internal-energy scheme with the presence of shocks, for the second test problem we consider a shock tube, as introduced by Sod (1978). At $t < 0$ a static, impermeable interface separates two states of a gas at rest. At $t = 0$ the barrier disappears, and a shock then forms. Because the problem admits a similarity solution that can be found exactly, it

is an ideal test problem for shocked flows. We test the performance of both the non-conservative, internal-energy scheme and the conservative, total-energy scheme.

The exact solution can be constructed as follows (Landau & Lifshitz 1987): Since neither the equations of motion nor the initial conditions contain a characteristic length, all interfaces must travel at constant speeds away from the initial discontinuity. A shock propagates into the low-pressure region; a rarefaction wave, into the high-pressure region. The gas between these two transitions travels at a constant speed and is uniform, except at a single point at which the density may be discontinuous, the contact discontinuity. The Rankine-Hugoniot jump conditions relate the upstream velocity, pressure, and density to the uniform middle region’s conditions. The transition across the rarefaction wave can be obtained by noting that the flow in this region is adiabatic, and so the physical quantities can be determined with the method of characteristics. Only one possible shock and one possible rarefaction wave allow the velocity and pressure to match in the middle region; we determine these numerically, since the relations are implicit.

With the exact solution in hand, we can test both internal-energy and total-energy schemes. We use Sod’s initial conditions. On the left side of the grid, the pressure and density are given the values 1; on the right, the pressure is 1/10 and the density is 1/8. (At the interface we give these quantities their averaged values.) In this section only the equation of state is given by a $\gamma = 7/5$ ideal gas.

Figure 5 dramatically illustrates the failure of the internal-energy scheme. (In the shock-tube calculations, we use $L_1/\Delta x = L_2/\Delta x = 3/2$.) We show the density in the region around the shock jump at $t = 1$ and compare the results of the two numerical schemes with the exact solution. Although the computed solutions appear well-behaved and free of instabilities, two problems with the internal-energy solution are apparent: first, the shock transition is in the wrong place (the shock velocity is 0.2% too low), and second, the post-shock density is wrong (0.3% too high). Further, the total-energy scheme gets both of these right; aside from a small post-shock oscillation, it exhibits *no* numerical difficulties. In Figure 6 we show the total-energy error accrued by the internal-energy scheme at various resolutions, and again this diagnostic verifies that the scheme does not converge toward a correct solution.

In Figure 7 we show the Cauchy error measures $\epsilon_{\Delta x}[m]$ associated with both schemes’ calculations. For each, the errors decrease with decreasing gridsize; in fact, the quantities are almost identical. As before, however, we already know that the internal-energy scheme does *not* converge to the correct solution.

The *rate* of convergence appears *poorer* than $O(\Delta x)$. We trace this slow convergence to the presence of contact discontinuities, which can present special problems to numerical schemes. We observe the correct rate of convergence when we alter the initial conditions to remove the discontinuity. This change removes much of the shock-tube problem’s usefulness as a test problem, though, since the time evolution is no longer given by a similarity solution. (In the next section, in which we discuss rates of convergence, we use a test problem with smooth initial conditions

that does not contain contact discontinuities.)

Unlike shocks, contact discontinuities do not develop in smooth flow. Similarly, the smoothed regions that represent contact discontinuities do not tend to steepen. Thus effects of non-zero gridsize cause them to spread without limit, rather than toward some steady state. For a contact discontinuity in an isobaric medium, translating at a constant speed, no length or time scales enter except the width w of the representation and the gridsize Δx . Thus a scaling holds among w , Δx , and the time t : we may write that $w(\Delta x, 2t) = 2w(\Delta x/2, t)$. It is clear that if the representation spreads without limit, then at all times $w(\Delta x, 2t) > w(\Delta x, t)$ and so $w(\Delta x/2, t) > w(\Delta x, t)/2$. Since the Cauchy error accrued at these discontinuities is proportional to their widths, the Cauchy error cannot scale linearly with the gridsize Δx . (We might expect that this diffusion process would lead the width w to behave asymptotically [as $t \rightarrow \infty$] as $t^{1/2}$. Instead, however, using the total-energy scheme we find that a calculation involving only the advection of contact discontinuities suggests that asymptotically w varies as $t^{1/3}$.)

For the shock tube, as in the steepening wave, the internal-energy scheme appears stable and convergent but fails to converge toward a correct solution. The Lax-Wendroff theorem shows that the conservative, total-energy scheme should converge toward a correct solution, and all indications are that it does so.

In brief, when the artificial-viscous lengths L_1 and L_2 are proportional to the gridsize Δx , the calculations of our internal-energy scheme do not converge to the known shock-tube solution; while those of our total-energy scheme do approach the exact solution. This result reinforces our finding that the internal-energy scheme fails in the presence of shocks. Further, the Cauchy errors (21) for the (correct) total-energy scheme and the (errant) internal-energy scheme are nearly *indistinguishable*. Use of convergence tests alone cannot guarantee convergence to the correct solution.

5. Effects of Diffusion on Convergence

Since the internal-energy scheme is unreliable when shocks are present, we employ the total-energy scheme exclusively for our discussion of convergence rates. The diffusive effects of linear artificial viscosity introduces a noticeable amount of diffusion even to linear perturbations. We first discuss in some detail the impact on small, linear waves. Then we show the effect on convergence rates for a wall shock—a test problem containing both a shock and small-amplitude waves.

5.1. Linear examples

The presence of linear artificial viscosity can have a surprisingly large effect on the observed convergence rate. To illustrate these effects, we consider small-amplitude waves. First we exhibit convergence rates for calculations of such waves, and then show consistency between rates in this calculation and rates derived using an analytic treatment. Finally we comment on the viscous lengths necessary to yield convergence rates close to the expected asymptotic result.

For the numerical calculations, we take as initial conditions the right-moving wave (19–20) discussed above in section 3, with amplitude $\delta_0 = 0.05$ and width parameter $\Delta = 0.4$. We calculate to time $t = 0.6$ using the total-energy scheme with linear artificial viscosity only—the quadratic artificial viscous length L_2 is 0. Figure 8 shows the Cauchy errors $\epsilon[m]$. Note that instead of plotting $\epsilon_{\Delta x}[m]$ as a function of Δx (as in Figures 2, 4, and 7), here we show it as a function of the viscous length L_1 . The computations use $L_1/\Delta x = 4$, chosen so that the resolution is sufficiently high that purely numerical errors (as compared with infinitely resolved computations with those values of the viscous length L_1) are negligible. Note that as L_1 decreases the decrease of the errors tends toward the expected linear rate (cf. the line segment corresponding to $O(\Delta x)$ dependence), but only rather slowly. To quantify this tendency, for triplets of calculations we define $\beta(L_1) = \log(\epsilon_{2L_1}[m]/\epsilon_{L_1}[m])/\log 2$, which approximates the logarithmic derivative of ϵ_{L_1} with respect to L_1 . In the asymptotic regime, β approaches the order of accuracy. We show β as a function of L_1 in Figure 9. Note that even at the smallest value of L_1 , β is still rather far from the expected value of 1 even though almost two orders of magnitude separate L_1 from the problem’s natural length scale Δ .

A simple analytic model shows such convergence rates are a consequence of the diffusive effects of linear artificial viscosity. Consider the equations of motion (1–4) linearized about a constant background, which (in terms of the small quantities ρ_1 , v_1 , and P_1) read

$$\frac{\partial \rho_1}{\partial t} = -v_0 \frac{\partial \rho_1}{\partial x} - \rho_0 \frac{\partial v_1}{\partial x} \quad (22)$$

$$\frac{\partial v_1}{\partial t} = -v_0 \frac{\partial v_1}{\partial x} - \frac{1}{\rho_0} \frac{\partial P_1}{\partial x} + L_1 c_0 \frac{\partial^2 v_1}{\partial x^2} \quad (23)$$

$$\frac{\partial P_1}{\partial t} = -\gamma P_0 \frac{\partial v_1}{\partial x} - v_0 \frac{\partial P_1}{\partial x}. \quad (24)$$

(The background is specified by the constants v_0 , ρ_0 , P_0 , and $c_0 = (\gamma P_0/\rho_0)^{1/2}$. Note that L_1 is the linear viscous length, *not* a perturbation quantity.) We include the artificial-viscous terms, but to leading order in the small perturbations the quadratic artificial viscosity vanishes. In the *absence* of linear artificial viscosity ($L_1 = 0$) the linearized equations take the familiar Euler form, and the three coupled equations can be rewritten as three *decoupled* equations,

$$\frac{\partial \chi_1}{\partial t} = -v_0 \frac{\partial \chi_1}{\partial x} \quad (25)$$

$$\frac{\partial \chi_{2,3}}{\partial t} = -(v_0 \pm c_0) \frac{\partial \chi_{2,3}}{\partial x}, \quad (26)$$

where $\chi_1 = \rho_1 - P_1/c_0^2$ and $\chi_{2,3} = (P_1/c_0 \pm \rho_0 v_1)/(2c_0)$, for modes that propagate along the three characteristic paths, at speeds v_0 and $v_0 \pm c_0$. In the *presence* of linear artificial viscosity,

performing the analogous transformation leads to three still coupled equations:

$$\frac{\partial \chi_1}{\partial t} = -v_0 \frac{\partial \chi_1}{\partial x} \quad (27)$$

$$\frac{\partial \chi_2}{\partial t} = -(v_0 + c_0) \frac{\partial \chi_2}{\partial x} + \frac{L_1 c_0}{2} \frac{\partial^2}{\partial x^2} (\chi_2 - \chi_3) \quad (28)$$

$$\frac{\partial \chi_3}{\partial t} = -(v_0 - c_0) \frac{\partial \chi_3}{\partial x} + \frac{L_1 c_0}{2} \frac{\partial^2}{\partial x^2} (\chi_3 - \chi_2). \quad (29)$$

Note that χ_1 , the mode that remains still with respect to the background velocity v_0 , is unaffected by artificial viscosity. We next *assume* that (as in the wave example above) one of the remaining modes is sufficiently larger than the other two so that we can neglect their influence on its propagation. Calling it simply χ , we thus obtain the equation of motion

$$\frac{\partial \chi}{\partial t} + (v_0 \pm c_0) \frac{\partial \chi}{\partial x} = \frac{L_1 c_0}{2} \frac{\partial^2 \chi}{\partial x^2}. \quad (30)$$

The left-hand side of this equation describes just the advection of the quantity χ , so that (with the identification of the diffusion constant $\nu = L_1 c_0 / 2$) the equation is simply the heat diffusion equation

$$\frac{\partial \chi}{\partial t} = \nu \frac{\partial^2 \chi}{\partial y^2}, \quad (31)$$

for the quantity $\chi(y, t)$ in the frame of reference that moves at the speed $v_0 \pm c_0$.

We study the convergence of solutions of the heat equation (31) as the diffusion coefficient ν tends to zero. We consider the time evolution of a Gaussian pulse. An *exact* solution for $t > 0$ is

$$\chi(y, t; \nu) = A \left(\frac{\Delta_0^2}{4\nu t + \Delta_0^2} \right)^{1/2} e^{-y^2 / (4\nu t + \Delta_0^2)}. \quad (32)$$

where A is the initial ($t = 0$) amplitude and Δ_0 is the initial width of the pulse. With this solution it is straightforward to calculate the Cauchy error (at a fixed time t) associated with a sequence of solutions in which the viscous parameter ν varies. In Figure 10 we show the Cauchy error $\epsilon_\nu[\chi]$ evaluated at $t = 0.6$ using an amplitude $A = 0.05$ and width $\Delta_0 = 0.3$. (We choose different values for the width parameters in this treatment and in the calculations described above because the shape of the initial conditions differs.) Again the convergence rate β , shown in Figure 11, becomes close to the expected value of 1 only at quite small values of the diffusion ν . In the context of the flat background of the previous calculations, we require values of the viscous length $L_1 = 2\nu/c_0$ much smaller than the natural length scale Δ_0 to achieve values of β close to 1.

To determine how small the diffusion coefficient ν —or, equivalently, the viscous length L_1 —must be in order to achieve a convergence rate β close to the asymptotic value of 1, we examine the *pointwise* convergence of the exact solution (32) of the linearized problem. That is, for any values of (y, t) , consider the behavior of $\chi(y, t; \nu)$ as $\nu \rightarrow 0$. We assume that, for sufficiently small values of ν , we may approximate

$$\chi(y, t; \nu) - \chi(y, t; 0) \approx \nu \frac{\partial \chi}{\partial \nu}(y, t; 0) + \frac{\nu^2}{2} \frac{\partial^2 \chi}{\partial \nu^2}(y, t; 0). \quad (33)$$

We determine the value of $\nu = \bar{\nu}(y, t)$ at which the first and second terms on the right-hand side are equal. The asymptotic regime for convergence lies at values of ν much less than $\bar{\nu}$. The calculation itself is elementary and yields

$$\bar{\nu}(y, t) = \frac{\Delta_0^2}{t} \left| \frac{2y^2 - \Delta_0^2}{4y^4 - 12y^2\Delta_0^2 + 3\Delta_0^4} \right| \quad (34)$$

The analogous quantity for the viscous length is

$$\bar{L}_1(y, t) = \Delta_0 \frac{\Delta_0}{c_0 t} \left| \frac{4\Delta_0^2 y^2 - 2\Delta_0^4}{4y^4 - 12y^2\Delta_0^2 + 3\Delta_0^4} \right| \quad (35)$$

Loosely, the convergence rate for the Cauchy error is a weighted (spatial) average of the pointwise convergence rate. Since the main contribution to the error comes from a region within a few widths Δ_0 of the spatial origin, we replace the dimensionless ratio in equation (35) by $1/2$. Thus, the asymptotic regime for the Cauchy error should lie at values of the viscous length L_1 much less than

$$\bar{L}_1 \approx \frac{\Delta_0}{2} \frac{\Delta_0}{c_0 t}. \quad (36)$$

Note that *smaller* values of L_1 are required as the time t increases to achieve the same convergence rate.

In practice, one may wish to increase the resolution of a computation until the convergence rate β is within some tolerance ε of the asymptotic value (here, 1). Assume [as above, in equation (33)] that for small L the error behaves as

$$\epsilon_L \propto \bar{L}L \pm L^2, \quad (37)$$

where \bar{L} specifies the value of L at which the two terms on the right-hand side contribute equally. The logarithmic derivative of the error ϵ_L with respect to L is then simply

$$\frac{L}{\epsilon_L} \frac{d\epsilon_L}{dL} = \frac{1 \pm 2L/\bar{L}}{1 \pm L/\bar{L}} \approx 1 \pm L/\bar{L}. \quad (38)$$

To attain a convergence rate within ε of 1, we must use values of L less than approximately $\varepsilon\bar{L}$. (Comparison with the results shown in Figures 9 and 11 suggest that this estimate is about right for the analytic model and too high for the numerical calculations by a factor of a few.)

5.2. Wall Shock

As noted above, even for the reliable total-energy scheme our results for the shock-tube problem do not yield the expected $O(\Delta x)$ rate of convergence. This is a consequence of the shock

tube’s discontinuous initial conditions. For our final test problem, we choose one that contains a shock, smooth initial conditions, and small-amplitude waves: a wall shock.

Gas impinges on a wall at $x = 0$. For uniform, supersonic flow from the right ($x > 0$), a shock will form and move outward. For initial conditions we place a transition between density, momentum, and energy values appropriate to a Mach 2 steady-state shock. (In the equation of state we again use $\gamma = 5/3$, as in the study of the nonlinear sound wave.) We mediate between upstream and downstream states with a smooth transition function:

$$v(x) = f(0, -9/8; x) \tag{39}$$

$$P(x) = f(57/20, 3/5; x) \tag{40}$$

$$\rho(x) = f(16/7, 1; x), \tag{41}$$

where the transition function is

$$f(a, b; x) = \begin{cases} a, & \text{if } x < 3 \\ (a + b)/2 + [(b - a)/2] \tanh \frac{35}{12}(x - 6), & \text{if } 3 < x < 9 \\ b, & \text{if } x > 9. \end{cases} \tag{42}$$

At the left edge (at $x = 0$) we use reflecting boundary conditions, but for the tests reported here we stop the calculations at $T = 2$ before any physical perturbations reach either edge of the computational grid.

Although the initial conditions do not represent the exact, steady-state profile for a shock transition, one quickly forms and translates away from the wall. Waves form and propagate away from the shock toward the wall. Figure 12 shows these structures in the density.

We have performed many calculations parameterized by the viscous length $L_1 = L_2 = L$ and the gridsize Δx . We use these to form two types of sequences: first, with the viscous parameter $L/\Delta x$ held constant, and second, with the viscous length L held constant as Δx varies.

Figure 13 shows the Cauchy error $\epsilon_{\Delta x}[m]$, again as a function of the viscous length L . Each of the five solid lines represents a sequence with constant $L/\Delta x$ ($= 1, 2, 4, 8, 16$). First, note that over the range of gridsizes Δx in which we can reasonably calculate, the convergence rate tends toward $O(\Delta x)$ but does not approach it unambiguously. Note also that the magnitude of the errors is almost entirely a function of the viscous *length* L —the solid lines overlap. That is, the particular choice of gridsize has only a small effect on the Cauchy error. The difficulty of achieving the expected convergence rate in these sequences must be an effect of the changing values of the viscous lengths, not of the finite resolution.

We attempt to isolate the effect of the shock transition on the Cauchy error by changing the limits of integration in its definition (21) to include only the transition region or to exclude it. Figure 13 also shows in dotted lines the error associated with the transition region ($x > 7$), and in dashed lines with the transients in the rest of the flow ($x < 7$). Note that the transition region yields the expected $O(\Delta x)$ convergence rate at relatively large values of the gridsize Δx . The

more slowly decreasing contribution to the Cauchy error appears in the region of the transients. The Cauchy error for the shock transition should asymptotically be proportional to the viscous length L , as discussed above, and so its convergence rate implies that transition widths are indeed scaling with L . (Appendix C discusses the small deviations from exact scaling in shock transition regions.)

Figure 14 shows again Cauchy errors as a function of gridsize Δx . Here, however, each solid line represents a set of calculations with a *fixed* value of the viscous length L . We show only calculations with the gridsize Δx sufficiently small that the timestep Δt is always determined by the diffusion condition (17); then the errors should (asymptotically) be $O((\Delta x)^2)$. It is clear that these calculations lie in the asymptotic regime: the errors are nearly proportional to $(\Delta x)^2$.

We use the *same* calculations to construct Figures 13 and 14. When considered as part of sequences with constant L , they unambiguously lie in the asymptotic regime; whereas when considered as part of sequences with constant $L/\Delta x$ they do *not*. We illustrate this dichotomy in Figure 15: each circle represents a calculation, and lines represent the sequences to which each belongs. For triplets of calculations in sequences, we calculate the numerical convergence rate $\beta(\Delta x) = \log(\epsilon_{2\Delta x}[m]/\epsilon_{\Delta x}[m])/\log 2$, which approaches the order of accuracy in the asymptotic regime. Values of $\beta(\Delta x)$ are shown on the lines that define the appropriate sequences of calculations. For each constant- L sequence, where we expect the errors to behave asymptotically as $O((\Delta x)^2)$, we find that $\beta = 2$ to several decimal places. For sequences of $L/\Delta x = \text{constant}$ calculations the closest we can achieve to the expected value ($\beta = 1$) is $\beta = 0.93$.

The Cauchy errors in the $L/\Delta x = \text{constant}$ sequences are larger in magnitude than those in the constant- L sequences (compare Figures 13 and 14). The smallness of the latter errors and the attainment of the expected convergence rate shows that errors in the former sequences are dominated by the effects of changing viscous lengths, *not* of insufficient resolution.

The apparently poor convergence rate in the post-shock region can be related (at least in part) to the discussion of small-amplitude waves above in section 5.1. The features in the post-shock region (cf. Figure 12) consist of relatively small-amplitude waves. A considerable contribution to the integrand defining the Cauchy error (21) comes from the region near $x = 3$, where a left-moving wave lies. From the previous discussion, for this wave alone we require much smaller viscous lengths L to attain a numerical convergence rate β within a few percent of 1. (We have deemed this to be computationally infeasible.)

This explanation implicitly assumes that the waves generated as the shock forms do not vary with the viscous length L . The width of the shock transition, varies as the viscous length, however, and so some post-shock waves (also varying as $O(L)$) must arise from the different transition widths. Along a sequence in which $L/\Delta x = \text{constant}$, these waves with short length scale should make a contribution of order $O(\Delta x)$ to the Cauchy error. The effect of the other (long length scale) waves on the numerical convergence rate continues to increase with time (i.e., β is further from 1), and so ultimately the effect of these should be greater than that of the short-wavelength

waves.

By studying this relatively simple test problem, we find that we can readily attain the expected $O((\Delta x)^2)$ convergence rate in sequences in which the viscous lengths L_1 and L_2 are constants. We emphasize that in such sequences the $\Delta x \rightarrow 0$ limit does *not* correspond to the Euler equations (1–4). In sequences in which the ratios $L_1/\Delta x$ and $L_2/\Delta x$ are constants, attaining the expected $O(\Delta x)$ convergence rate appears more difficult. The difficulty is tied to the changes in viscous lengths, not to numerical errors introduced by non-zero gridsizes. We attribute it to the diffusive effects of linear artificial viscosity on waves that are generated as the shock forms.

6. Conclusions

We have investigated the use of convergence tests to assess the accuracy of finite-difference solutions to the Euler equations in the presence of shocks. We find that a non-conservative internal-energy scheme does not converge to solutions of the continuum equations. Use of the Cauchy error does *not* detect this significant failure. The Lax-Wendroff theorem applies to our total-energy scheme (as shown in Appendix A), however, and so it provides reliable results.

Our identification of this failure with the presence of shocks leads us to introduce a modification of the equations of motion, in which the artificial-viscous terms are held constant as the gridsize varies, rather than scaled with the gridsize. In such modified systems, smooth transitions replace shock discontinuities. With the discontinuities removed, the internal-energy scheme converges as expected, without the indications of the problems that signal the failure of the unmodified system.

For well-behaved schemes, convergence at the expected rate can be used as a clear indicator of accuracy, a particularly unambiguous criterion in automated contexts. Diffusion due to linear artificial viscosity can lead to convergence difficulties. By investigating a wall shock with smooth initial conditions, however, using our definition of Cauchy error to provide the criterion for convergence, we readily achieve the expected convergence rate when the artificial-viscous terms are held constant, and approach it when the artificial-viscous terms vanish with the gridsize.

Finally, we have investigated the possibility of using the calculations that establish our numerical convergence rate in extrapolations. In sequences in which the artificial viscosity scales with the gridsize, we find that transitions that represent shocks deviate in several ways from exact scaling. Our findings on extrapolations and scaling can be found in Appendix C.

We wish to thank Sam Finn, Matt Choptuik, John Hawley, Mordecai Mac Low, Jim Stone, and Paul Woodward for helpful discussions. This research has been carried out at Cornell University with the generous support of the NSF (AST-8657467) under the PYI program

and NASA (NAGW-2224) under the LTSA program. PAK wishes further to acknowledge the support of an NSF Graduate Fellowship. Some computations reported herein were carried out using the resources of the Cornell Theory Center, which receives major funding from the NSF and IBM Corporation, with additional support from New York State Science and Technology Foundation and members of its Corporate Research Institute.

A. Lax-Wendroff Theorem, Extended

We discuss in this appendix the extension of the Lax-Wendroff theorem to multi-step, operator-split schemes. This theorem was originally presented by Lax and Wendroff (1960); our discussion follows their treatment.

Write the system of conservation laws as

$$\frac{\partial u}{\partial t} = \frac{\partial f}{\partial x}, \quad (\text{A1})$$

where u is an unknown vector function of x and t and f is a given vector function of u . The theorem requires that the difference equations be written in the form

$$v(x, t + \Delta t) = v(x, t) + \frac{\Delta t}{\Delta x} \Delta g, \quad (\text{A2})$$

where $\Delta g = g(x + \Delta x/2) - g(x - \Delta x/2)$. The numerical flux g is determined in the following fashion: $g(x + \Delta x/2) = G(v_{-l+1}, v_{-l+2}, \dots, v_l)$, where G is a vector-valued function of $2l$ vector arguments, which is related to f by the *single* requirement that G approach f , in the sense that

$$\lim_{\text{all } v_j \rightarrow v} G(v_1, v_2, \dots, v_{2l}) = f(v). \quad (\text{A3})$$

If, in the limit $\Delta x, \Delta t \rightarrow 0$, $v(x, t)$ converges (boundedly, almost everywhere) to some function $u(x, t)$, then $u(x, t)$ is a weak solution of (A1).

We claim that the proof also holds if the numerical flux g is given by a vector-valued function G of vector arguments and a (scalar) parameter, $\lambda = \Delta t/\Delta x$, such that

$$\lim_{\text{all } v_j \rightarrow v, \lambda \rightarrow \text{const.}} G(v_1, v_2, \dots, v_{2l}; \lambda) = f(v). \quad (\text{A4})$$

Operator-split schemes satisfy this condition, as we now explain. Write the continuum equations (A1) as

$$\frac{\partial u}{\partial t} = \frac{\partial f^{(1)}}{\partial x} + \frac{\partial f^{(2)}}{\partial x}, \quad (\text{A5})$$

where we take the number of substeps to be 2 (for notational simplicity). The difference equations will consist of two substeps to represent the equations

$$\frac{\partial u}{\partial t} = \frac{\partial f^{(1)}}{\partial x} \quad (\text{A6})$$

$$\frac{\partial u}{\partial t} = \frac{\partial f^{(2)}}{\partial x} \quad (\text{A7})$$

sequentially. That is, the first substep takes the form

$$\tilde{v}_j = v_j + \frac{\Delta t}{\Delta x} \Delta g^{(1)}(\{v_j\}), \quad (\text{A8})$$

where $\{v_j\}$ represents the set of all relevant v_j . The resulting set $\{\tilde{v}_j\}$ enters the second substep

$$v_j^1 = \tilde{v}_j + \frac{\Delta t}{\Delta x} \Delta g^{(2)}(\{\tilde{v}_j\}). \quad (\text{A9})$$

We assume that the substeps' numerical fluxes $g^{(1)}$ and $g^{(2)}$ are consistent with the substep fluxes $f^{(1)}$ and $f^{(2)}$ in the sense of (A3).

The split scheme can be rewritten in the awkward one-step form

$$v_j^1 = v_j + \frac{\Delta t}{\Delta x} \Delta g^{(1)}(\{v_j\}) + \frac{\Delta t}{\Delta x} \Delta g^{(2)}\left(\left\{v_j + \frac{\Delta t}{\Delta x} \Delta g^{(1)}(\{v_j\})\right\}\right) \quad (\text{A10})$$

$$= v_j + \frac{\Delta t}{\Delta x} \Delta \left[g^{(1)}(\{v_j\}) + g^{(2)}\left(\left\{v_j + \frac{\Delta t}{\Delta x} \Delta g^{(1)}(\{v_j\})\right\}\right) \right] \quad (\text{A11})$$

$$= v_j + \frac{\Delta t}{\Delta x} \Delta \mathcal{G}, \quad (\text{A12})$$

where $\mathcal{G}(\{v_j\}, \Delta t/\Delta x)$ is defined by the quantity in the square brackets.

Since the scheme can be written in the conservative form (A2), we now establish that the numerical flux \mathcal{G} satisfies the extended consistency requirement (A4). Let all of its vector arguments approach the value v , while $\Delta t/\Delta x$ approaches some constant, finite value. Then $\Delta g^{(1)}$ must vanish (since $g^{(1)}$ is a continuous function of its vector arguments where all of them are equal), and so essentially \mathcal{G} becomes $g^{(1)}(\{v_j\}) + g^{(2)}(\{v_j\})$. Since each of $g^{(1)}$ and $g^{(2)}$ are consistent with $f^{(1)}$ and $f^{(2)}$, then \mathcal{G} must be consistent with f .

B. Internal-Energy Scheme, Variations

In this appendix we describe changes made to the internal-energy scheme, whose basic form is given in section 2. We emphasize that *none* of these changes affects the conclusions of sections 3 and 4: the scheme still converges to solutions that are demonstrably incorrect.

1. The viscous lengths L_1 and L_2 and the timestep safety factors C and D were varied in ranges given.

parameter	range
L_1	0.1–1
L_2	1–32
C	0.3–0.9
D	0.008–0.9

2. A staggered grid allows cleaner implementation of the van Leer advection scheme. The vector quantities—velocity and momentum—are stored at gridpoints midway between the gridpoints

for the remaining (scalar) quantities. This requires that every difference equation be modified: Pressure acceleration (7) becomes

$$m_{j+1/2} \mapsto m_{j+1/2} - \frac{\Delta t}{\Delta x}(P_{j+1} - P_j). \quad (\text{B13})$$

The artificial-viscosity difference equations (8, 9) become

$$m_{j+1/2} \mapsto m_{j+1/2} - \frac{\Delta t}{\Delta x}(Q_{j+1} - Q_j) \quad (\text{B14})$$

$$(e_{int})_j \mapsto (e_{int})_j - \frac{\Delta t}{\Delta x}Q_j(v_{j+1/2} - v_{j-1/2}), \quad (\text{B15})$$

where now $(\partial v/\partial x)_j = (v_{j+1/2} - v_{j-1/2})/\Delta x$. The compressional heating equation (11) becomes

$$(e_{int})_j \mapsto (e_{int})_j - \frac{\Delta t}{\Delta x}P_j(v_{j+1/2} - v_{j-1/2}). \quad (\text{B16})$$

The van Leer advection procedure is virtually unchanged for scalar quantities. The velocity at the staggered gridpoints is taken to be $v_{j+1/2} = 2m_{j+1/2}/(\rho_j + \rho_{j+1})$. For the momentum (a vector quantity), the velocity at the other gridpoints is taken to be $v_j = (m_{j-1/2} + m_{j+1/2})/(2\rho_j)$.

3. As in Norman and Winkler (1986) and Stone and Norman (1992), the pressure-acceleration term in the momentum equation (2) can be replaced by

$$\frac{\partial v}{\partial t} = -\frac{1}{\rho} \frac{\partial P}{\partial x}. \quad (\text{B17})$$

The difference equation for the physical pressure (B13) must be replaced by

$$v_{j+1/2} \mapsto v_{j+1/2} - \frac{2\Delta t}{\Delta x} \frac{P_{j+1} - P_j}{\rho_{j+1} + \rho_j}, \quad (\text{B18})$$

and that for the artificial-viscosity term (B14), by

$$v_{j+1/2} \mapsto v_{j+1/2} - \frac{2\Delta t}{\Delta x} \frac{Q_{j+1} - Q_j}{\rho_{j+1} + \rho_j}. \quad (\text{B19})$$

4. In Norman and Winkler (1986) and Stone and Norman (1992), energy conservation is improved by using a “time-centered pressure” (as in $P^{n+1/2} = (P^n + P^{n+1})/2$) on the right-hand side of the compressional-heating term of the internal-energy equation (3), then applying the equation of state to replace the pressure with the internal-energy density. The substep then can be expressed as

$$(e_{int})_j \mapsto (e_{int})_j \frac{1 - \Delta t(\gamma - 1)(v_{j+1/2} - v_{j-1/2})/2\Delta x}{1 + \Delta t(\gamma - 1)(v_{j+1/2} - v_{j-1/2})/2\Delta x}, \quad (\text{B20})$$

which replaces (11).

5. Consistent-transport advection (Norman, Wilson & Barton 1980) is said to improve local conservation of certain quantities. The advection of mass density remains the same. The remaining quantities are treated “consistently” with the mass density. In the van Leer advection substep, the momentum, rather than the velocity, moves the quantities over the grid. In the procedure for calculating the fluxes $\mathcal{F}_{j+1/2}$, the momentum density field replaces the velocity field, and (to compensate for the extra factor of mass density) the specific densities ψ/ρ replace the densities ψ themselves.

C. Extrapolation and Transition-Region Scaling

In the main body of this paper, we adopt the attitude that we may regard a calculation as reliable if we can show that it lies within the asymptotic regime (i.e., if its errors are converging as expected). Since such a determination uses several calculations at different gridsizes, it is then straightforward to attempt to calculate an even more accurate solution by extrapolating the set of calculations.

We first consider the wall-shock problem of section 5.2. Because its physical structure is relatively simple—one shock wave and detached waves—we investigate the possibility of using the many calculations to perform extrapolations to the $\Delta x \rightarrow 0$ limit. Where the flow is smooth, an extrapolation in powers of the gridsize Δx is valid. If the calculations extend into the asymptotic regime, then the extrapolations should be quite accurate.

C.1. Extrapolation at constant L

First, consider extrapolations of sequences in which the viscous lengths L_1 and L_2 are held constant. We use calculations for which timesteps Δt are proportional to $(\Delta x)^2$; then the truncation error associated with each is of order $O((\Delta x)^2)$. We assume that, at each gridpoint in the best-resolved calculation, the results can be expressed as

$$\psi_{\Delta x}(x, T) = \psi(x, T) + a_2(\Delta x)^2 + a_3(\Delta x)^3 + \dots, \quad (\text{C21})$$

with some coefficients $a_n = a_n(x, T)$ (Richardson & Gaunt 1927). (The linear term is absent because the scheme is second-order.) Extrapolation of N calculations finds the value of $\psi(x, T) = \psi_{\Delta x=0}(x, T)$ by eliminating the first $N - 1$ error terms. Where values are required from calculations at points other than gridpoints, we interpolate using polynomials to an order of accuracy at least that of the eventual extrapolated result. The extrapolations are well-behaved and apparently more accurate than their component calculations. We illustrate this accuracy in

Figure 16 by means of a Cauchy error obtained using extrapolations. The extrapolations, for which $L_1 = L_2 = L = 1/8$, use calculations (with gridsizes differing by factors of 2) from $\Delta x = 1/16$ down to the value of the gridsize indicated on the horizontal axis. The error decreases markedly with increasing resolution (which also corresponds to more extensive extrapolation).

C.2. Extrapolation at constant $L/\Delta x$

Next, consider extrapolations in which the viscous parameter $L_1/\Delta x = L_2/\Delta x = L/\Delta x$ is held constant. (For these extrapolations we assume that the errors take a form similar to that in equation (C21), but *include* the term linear in the gridsize Δx , because of the first-order accuracy.) Figure 17 shows the density as extrapolated from a sequence with $L/\Delta x = 2$. (This sequence includes the calculation illustrated above in Figure 12.) Qualitatively, the results appear poor in the region of the shock, but sensible in the remainder of the flow. The sharp features of the waves are ungarbled by the extrapolation, even though some features must result from the formation of the shock discontinuity. In the shock region, representations of shocks approach discontinuities in the $\Delta x \rightarrow 0$ limit. Hence, although the Cauchy error measure $\epsilon_{\Delta x}[\psi]$ for the entire flow approaches the expected $O(\Delta x)$ behavior, near the shock the pointwise behavior of the error *cannot* lie in the asymptotic regime.

C.3. Transitions in shock regions

Although pointwise extrapolation of a sequence of calculations fails near shocks when the viscous lengths L_1 and L_2 change within the sequence, one might try to devise a special procedure for extrapolation in shock regions. Any such method must consider the expected scaling of the transition region with the viscous lengths. We investigate the mechanisms that alter this scaling. We begin with a steady-state problem, the shock tube, to investigate short length scales, then move to the wall-shock problem for the influence of large-scale gradients.

Consider a *steady-state* shock with uniform upstream and downstream conditions. The shock travels at constant speed, and the transition width for the shock representation must be determined by the viscous lengths L_1 and L_2 . For simplicity, we take $L_1 = L_2 = L$. Transitions calculated at different viscous lengths L then are related by a scaling relation:

$$\psi(x, t; L) = \tilde{\psi}\left(\frac{x - x_s(t)}{L}\right) \tag{C22}$$

in the region of the shock, located at x_s , where the function $\tilde{\psi}$ is independent of L .

Given two calculations $\psi^{(1)}(x, t)$ and $\psi^{(2)}(x, t)$ made with different gridsizes Δx , viscous lengths L , or both, we measure the deviation from exact scaling by means of the function

$$D^{(1,2)}[\psi](\xi, t) = \psi_{\Delta x^{(1)}}^{(1)}(x_s^{(1)} + L^{(1)}\xi, t) - \psi_{\Delta x^{(2)}}^{(2)}(x_s^{(2)} + L^{(2)}\xi, t) \quad (\text{C23})$$

in the vicinity of $\xi = 0$. Calculating this deviation function requires knowing the shock positions $x_s^{(1)}$ and $x_s^{(2)}$. In practice, when comparing computations with different viscous lengths L , we assume that $x_s^{(1)} = x_s^{(2)}$ and approximate the shock position by locating the intersection of the two shock representations. Determining x_s in other ways does not change our results significantly. The deviation function vanishes if the calculations obey the exact scaling relation (C22), since then $\psi^{(1)}(x_s^{(1)} + L^{(1)}\xi, t) = \psi^{(2)}(x_s^{(2)} + L^{(2)}\xi, t) = \tilde{\psi}(\xi)$. When it is more convenient to work with a scalar deviation measure, we calculate a norm of $D[\psi](\xi)$:

$$\left\| D^{(1,2)}[\psi] \right\| = \int_{-\eta}^{\eta} \left| D^{(1,2)}[\psi](\xi) \right| d\xi. \quad (\text{C24})$$

To limit the investigation to the shock region, the parameter η should not be chosen too large; we take $\eta = 5$.

We begin our discussion of deviations from scaling with the shock-tube problem, in which the shock is truly steady-state. Our comparisons of calculations fall into two categories: first, we compare calculations with the *same* viscous length L ; and, second, we compare calculations with *different* values of L . In the second type, comparisons between calculations with the *same* value of the ratio $L/\Delta x$ are a useful special case. (For illustrations we focus on the sequence with $L/\Delta x = 4$.)

Before describing the causes of scaling deviations, we first discuss some useful properties of shock-tube calculations. In this problem the only length scale set by initial conditions and equations of motion is the artificial-viscous length L . Thus solutions of the continuum equations (including the effects of artificial viscosity) obey the scaling property

$$\psi(x, t; L) = \psi(\sigma x, \sigma t; \sigma L), \quad (\text{C25})$$

with σ arbitrary, where the spatial origin is chosen at the point of the initial discontinuity. The corresponding finite-difference solutions have an analogous property. A difference solution $\psi_j^n = \psi_{\Delta x}(j\Delta x, t_n; L)$, which approximates the continuum solution $\psi_L(j\Delta x, t_n)$, may equally well be interpreted as the result of a calculation in which the values of the viscous length L , the gridsize Δx , and the timesteps Δt are all scaled by σ : $\psi_j^n = \psi_{\sigma\Delta x}(j\sigma\Delta x, \sigma t_n; \sigma L)$. Hence, two calculations with the same value of the viscous parameter $L/\Delta x$ made to the same time T at different gridsizes $(\Delta x)_1$ and $(\Delta x)_2$ are completely equivalent to two calculations with the same $L/\Delta x$ and $(\Delta x)_1$, but made to the times T and $((\Delta x)_1/(\Delta x)_2)T$, respectively.

Truncation error (shock tube)

We have identified several causes of deviations from exact scaling. First, if the two viscous lengths entering into $D[\psi]$ are the same, then actually it does not measure deviations from scaling. Instead, it measures the truncation errors proportional to $(\Delta x)^2$ of computed solutions (as compared to the “exact” solution with that same *finite* value of L).

We estimate the magnitude of these truncation errors in a calculation at a given gridsize Δx by differencing it with a calculation at the smaller gridsize $\Delta x/2$ (with the same value of the viscous length L). In Figure 18 we show this estimate of truncation errors as a function of the scaled spatial coordinate $\xi = (x - x_s)/L$ in the shock-tube problem for calculations (to the fixed time $T = 1$) at gridsizes $\Delta x = 1/100, 1/200, 1/400, 1/800$, all with the viscous length L chosen so that $L/\Delta x = 4$. Note that the results are all quite similar despite the different values of L and Δx . Along a sequence in which $L/\Delta x = \text{constant}$, the effect of truncation error is a constant in the scaled coordinate ξ .

We explain this result as follows: Interpret the results as a sequence in *time* of truncation errors at a single gridsize and viscous length. If this chosen gridsize is $\Delta x = 1/800$, then Figure 18 shows results at times $t = 1/8, 1/4, 1/2$, and 1, respectively. It then indicates that when the transition is near steady-state, the truncation error remains nearly constant in time.

Time-dependent relaxation (shock tube)

The solid line in Figure 19 shows the deviation function $D[\rho]$ that compares transitions calculated with viscous lengths $L^{(1)} = 1/25$ and $L^{(2)} = 1/50$, with the gridsize chosen sufficiently small ($\Delta x = 1/1600$) so that the $O((\Delta x)^2)$ truncation errors are small. This illustrates a second source of deviations from exact scaling. We identify it as an approach to steady state, as the discontinuous initial conditions relax toward a steady-state computed transition. (The shape of the functions in Figure 19 show that transitions are steeper than the idealized, scaling case.) This relaxation is a consequence of the artificial viscosity, and so it is reasonable that its time scale must be on the order of L/u (where u is some characteristic velocity), which is the only time scale available in the problem. (Alternatively, we may argue that the diffusion time scale for a length ℓ is on the order of ℓ^2/\mathcal{D} , with diffusion coefficient $\mathcal{D} \propto uL$. Since the computed transition width evolves from zero to a value on the order of L , the resulting time scale is on the order of L/u .) When the ratio L/T is smaller, the transition should be closer to steady state [i.e., the exact-scaling transition function (C22)].

Figure 19 also shows (dashed line) the deviation function calculated with the same values of the viscous length L but with larger gridsizes, chosen with the same value of the ratio $L/\Delta x = 4$. With such large gridsizes, the $O((\Delta x)^2)$ truncation error associated with either calculation is much larger in magnitude than the deviation function. The deviation function, however, is nearly identical to that in the more accurate, small-gridsize calculations. This shows a consequence of the similarity in truncation errors as a function of $\xi = (x - x_s)/L$ along sequences with fixed $L/\Delta x$:

Write the result of a calculation at gridsize Δx and viscous length L in the vicinity of the shock as

$$\psi_{\Delta x}(x, t; L) = \psi(x, t; L) + \mathcal{T}\left(\frac{x - x_s}{L}, t; \frac{L}{\Delta x}\right), \quad (\text{C26})$$

where the truncation error \mathcal{T} depends on Δx through the ratio $L/\Delta x$, as discussed above. Then the deviation function for calculations with the *same value* of $L/\Delta x$ reduces to

$$\begin{aligned} D^{(1,2)}[\psi](\xi) &= \psi^{(1)}(x_s + L^{(1)}\xi, t; L^{(1)}) + \mathcal{T}\left(\xi, t; \frac{L}{\Delta x}\right) \\ &\quad - \psi^{(2)}(x_s + L^{(2)}\xi, t; L^{(1)}) - \mathcal{T}\left(\xi, t; \frac{L}{\Delta x}\right) \\ &= \psi^{(1)}(x_s + L^{(1)}\xi, t; L^{(1)}) - \psi^{(2)}(x_s + L^{(2)}\xi, t; L^{(1)}), \end{aligned} \quad (\text{C27})$$

that is, the deviation function for calculations without truncation errors.

We use this result to determine $\Delta x \rightarrow 0$ deviation functions over a wide range of viscous lengths L , including values of L for which sufficiently accurate calculations (i.e., with small truncation errors) are computationally infeasible. In Figure 20 we show the scalar deviation measure (C24) as a function of L , determined from a sequence of calculations at gridsizes $\Delta x = 1/100, 1/200, \dots, 1/3200$, with $L/\Delta x = 4$. In the reinterpretation of these calculations as a sequence in increasing *time* (rather than increasing *resolution*), we have a sequence at times $t = 1/32, 1/16, \dots, 1$. Because the deviations result from a diffusive relaxation process, we naïvely expect their amplitudes to decrease exponentially with increasing time (or decreasing L). Clearly the deviations decrease, but not exponentially. (The behavior appears more similar to a power law, but it does not approach one asymptotically. In any case, we have no reason to expect such behavior.)

Morduchow and Paullay (1971) and Morduchow and Valentino (1979), working with a one-dimensional ideal gas with a Prandtl number of $3/4$, performed an eigenvalue analysis to investigate shock stability. They found a continuum of decay rates, including values arbitrarily close to zero. If our system shares this property, then even asymptotically we should not expect to observe exponential decay. A combination of perturbation modes with a continuum of rates could imitate the observed behavior.

Large-scale gradients (wall shock)

Our third and last cause of deviations from exact scaling has a simple physical origin. Large-scale gradients in the flow have an effect on the structure of the transition. Since transitions of different widths sample these gradients to different extents, observable deviations result. To illustrate, we consider a physical problem in which the shock itself is not in steady state, the wall-shock problem. Although as $t \rightarrow \infty$ the shock approaches steady state, at any finite time the shock generates weak gradients in the downstream region.

Figure 21 shows deviation functions $D[\rho](\xi)$ for the wall-shock problem. The two curves represent comparisons of, first (solid line), $L^{(1)} = 1/128$ and $L^{(2)} = 1/256$ (using $L/\Delta x = 8$), and second (dashed line), $L^{(1)} = 1/256$ and $L^{(2)} = 1/512$ (using $L/\Delta x = 4$). (The sense of the deviation shows that the transition is steepening; this agrees with the smoothed initial conditions, which [by design] are less steep than the steady-state transition.) Note the effect of the large-scale gradients downstream from the shock—unlike in the steady-state, shock-tube cases, $D(\xi)$ tends toward non-zero values for negative values of $\xi = (x - x_s)/L$. The slope (with respect to ξ) with which the curve turns away from zero on the left side should be proportional to the scaling factor, i.e., L , as Figure 21 verifies.

C.4. Extrapolation difficulties

Our investigations into extrapolation procedures suggest difficulties in devising an automated extrapolation scheme that ensures a predetermined order of accuracy. Extrapolating sequences with the artificial-viscous length L fixed appears feasible, but the improvements are small. Direct pointwise extrapolation of sequences in which the viscous length L is chosen proportional to the gridsize Δx yields improvements away from shocks, but at the cost of reasonable behavior at shocks. Finally, our studies of the scaling behavior of shock transitions suggests that computed transitions in general deviate from exact scaling behavior in ways not easily controlled; exploiting the scaling behavior to extrapolate to zero-width shock transitions may incur errors of unknown magnitude.

REFERENCES

- Finn, L. S. and Hawley, J. F. 1989, unpublished report.
- Hawley, J. F., Smarr, L. L. and Wilson, J. R. 1984, *ApJS*, 55, 211.
- Landau, L. D. and Lifshitz, E. M. 1987, *Fluid Mechanics*, second edition, translated by J. B. Sykes and W. H. Reid (Oxford: Pergamon).
- Lax, P. and Wendroff, B. 1960, *Comm. Pure Appl. Math.*, 13, 217.
- Morduchow, M. and Paullay, A. J. 1971, *Phys. Fluids*, 14, 323.
- Morduchow, M. and Valentino, J. V. 1979, *J. Appl. Mech.*, 46, 505.
- Norman, M. L., Wilson, J. B. and Barton, R. T. 1980, *ApJ*, 239, 968.
- Norman, M. L. and Winkler, K.-H. A. 1986, 2-D Eulerian Hydrodynamics with Fluid Interfaces, Self-Gravity and Rotation, in *Astrophysical Radiation Hydrodynamics*, edited by M. L. Norman and K.-H. A. Winkler (Dordrecht: Reidel), p. 187.
- Richardson, L. F. and Gaunt, J. A. 1927, *Phil. Trans. Roy. Soc. Lond. A*, 226, 299.
- Richtmyer, R. D. and Morton, K. W. 1967, *Difference Methods for Initial-Value Problems*, second edition (New York: Interscience).
- Sod, G. A. 1978, *J. Comput. Phys.*, 27, 1.
- Sod, G. A. 1985, *Numerical Methods in Fluid Dynamics: Initial and Initial Boundary-Value Problems* (Cambridge: Cambridge University Press).
- Stone, J. M. and Norman, M. L. 1992, *ApJS*, 80, 753.
- van Leer, B. 1977, *J. Comput. Phys.*, 23, 276.

Figure captions

1. Difference between total energy in an internal-energy computation and exact total energy, as a function of gridsize Δx in the steepening-wave problem of section 3. Artificial viscosity vanishes with decreasing gridsize. Each line corresponds to a different time (from bottom to top, $t = 4, 8, 12, \dots, 40$). When $t > 24$, the error does not tend toward zero.
2. Cauchy errors (21) for momentum density in the steepening-wave problem. The two lines correspond to $t = 20$ and $t = 40$.
3. Difference between total energy in an internal-energy computation and exact total energy, as a function of gridsize Δx in the steepening-wave problem. The viscous lengths L_1 and L_2 are fixed. Each line corresponds to a different time ($t = 4, 8, 12, \dots, 40$).
4. Cauchy errors for the steepening-wave problem. The viscous lengths L_1 and L_2 are fixed. The two lines correspond to $t = 20$ and $t = 40$.
5. The region near the shock front in the shock-tube problem calculated by both internal-energy (solid curve) and total-energy schemes (dashed curve) (at $t = 1$, using $\Delta x = 1/6400$ and $L_1 = L_2 = 3/12800$) as well as the exact solution (dotted curve).
6. Difference between total energy in an internal-energy computation of the shock tube and the exact total energy, as a function of gridsize Δx . Increased resolution does not yield a better result.
7. Momentum Cauchy errors for both internal-energy and total-energy calculations of the shock tube. Their behaviors are almost indistinguishable, although the internal-energy calculation is wrong.
8. Momentum Cauchy errors for a small-amplitude sound wave. The quadratic viscous length L_2 is zero. The linear viscous length L_1 is chosen to be $4\Delta x$. The short line segment indicates a slope corresponding to Δx dependence.
9. The numerical convergence rate β for a small-amplitude sound wave. The viscous lengths are $L_1 = 4\Delta x$ and $L_2 = 0$.
10. Cauchy errors for the analytic solution of the heat equation as diffusion coefficient $\nu \rightarrow 0$. As discussed in the text, the linearized equations of motion in the presence of linear artificial viscosity may take this form.
11. The numerical convergence rate β associated with solutions of the heat equation as $\nu \rightarrow 0$.
12. Density as a function of x for the wall-shock problem of section 5, at $t = 2$, computed with $L_1 = L_2 = 1/128$ at $\Delta x = 1/256$.

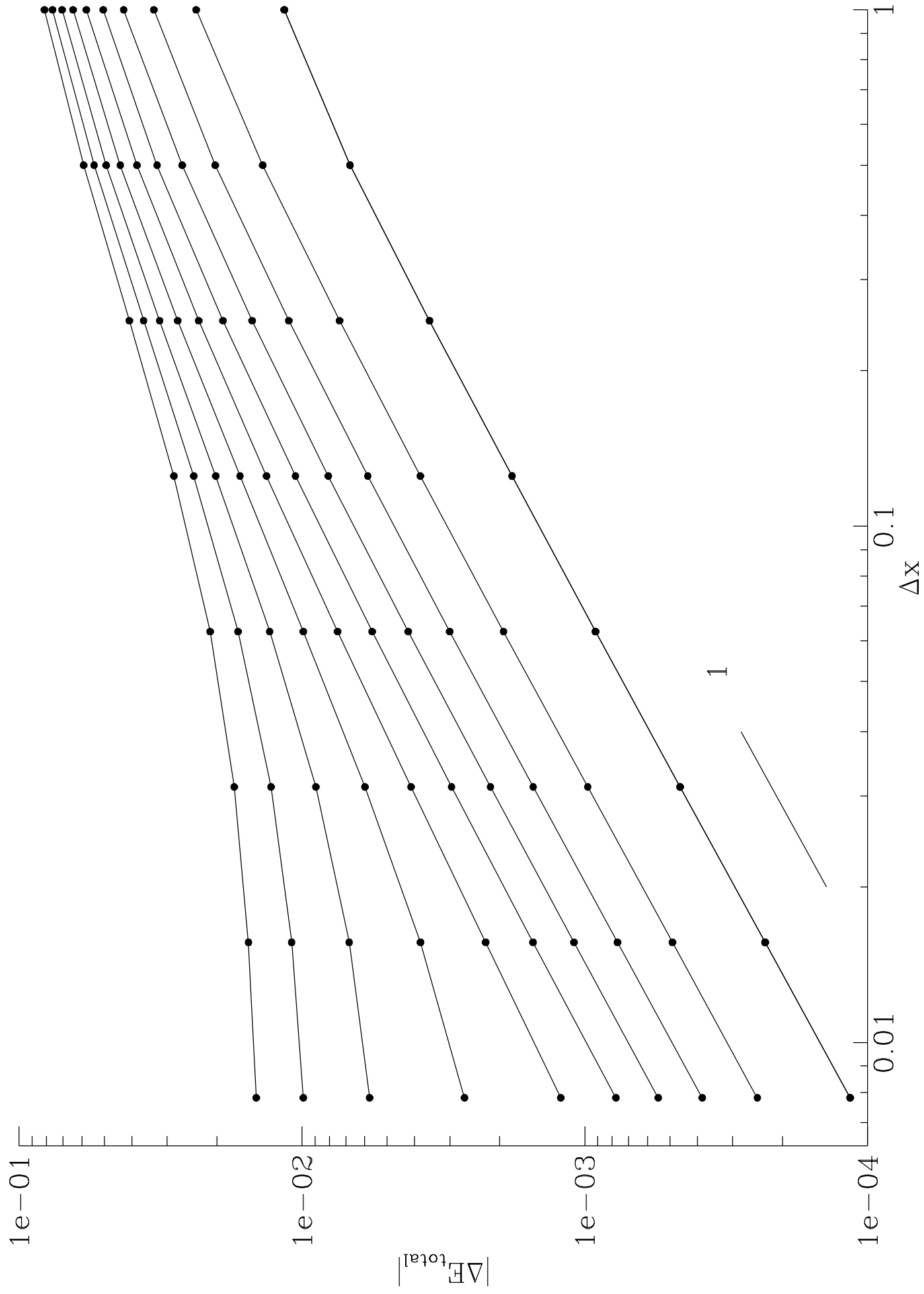
13. Momentum Cauchy errors for the wall-shock problem. Each solid line describes a sequence of calculations in which the viscous length $L_1 = L_2 = L$ is a constant multiple of the gridsize; five lines represent the values $L/\Delta x = 1, 2, 4, 8, 16$. The short line segment indicates a slope corresponding to Δx dependence. The dashed and dotted lines isolate the contributions from the shock-transition region ($x < 7$) and the rest of the flow ($x > 7$), respectively.
14. Momentum Cauchy errors for the wall-shock problem. Each line describes a sequence of calculations in which the viscous lengths $L_1 = L_2 = L$ are held constant (from left to right, $L = 1/256, 1/128, \dots, 1/8$).
15. Convergence of the momentum Cauchy errors for the wall-shock problem, considered within sequences in which the viscous lengths L_1 and L_2 are *constant* (horizontal lines) and *proportional to the gridsize* Δx (diagonals). Numerical convergence rates β , shown along these sequences, measure the approach to the expected convergence rates $O(\Delta x)$ and $O((\Delta x)^2)$.
16. Momentum Cauchy errors for extrapolations in the wall-shock problem, with $L = 1/8$. The extrapolations use calculations from $\Delta x = 1/16$ down to the value of the gridsize shown on the horizontal axis.
17. The result of a pointwise extrapolation of three calculations of the wall-shock problem, at gridsizes $\Delta x = 1/64, 1/128, 1/256$, with $L/\Delta x = 2$.
18. The $O((\Delta x)^2)$ truncation error (estimated as discussed in text) as a function of $\xi = (x - x_s)/L$ in the shock-tube problem at $t = 1$. The estimates are for four calculations, all with $L/\Delta x = 4$, with gridsizes $\Delta x = 1/100, 1/200, 1/400, 1/800$. As discussed in the text, these calculations may also be interpreted as a sequence in time ($t = 1/8, 1/4, 1/2, 1$) at $\Delta x = 1/800$.
19. Deviation from exact shock-transition scaling of density (C23) as a function of $\xi = (x - x_s)/L$ in the shock-tube problem. The solid line compares $L = 1/25$ and $L = 1/50$ calculations; the $O((\Delta x)^2)$ truncation error is negligible. The dashed line compares $L = 1/25, \Delta x = 1/100$ and $L = 1/50, \Delta x = 1/200$ calculations; the $O((\Delta x)^2)$ truncation error for either is larger in magnitude than the function plotted here.
20. Deviation from exact shock-transition scaling of density (C24) as a function of viscous length L . The $O((\Delta x)^2)$ truncation error has been removed, as described in the text, leaving the effects of relaxation toward exact scaling.
21. Deviation from exact shock-transition scaling of density (C23) as a function of $\xi = (x - x_s)/L$ for the wall-shock problem. The solid curve represents a comparison of $L = 1/128$ with $L = 1/256$; the dashed curve, of $L = 1/256$ with $L = 1/512$.

This figure "fig1-1.png" is available in "png" format from:

<http://arxiv.org/ps/astro-ph/9311019v1>

This figure "fig2-1.png" is available in "png" format from:

<http://arxiv.org/ps/astro-ph/9311019v1>

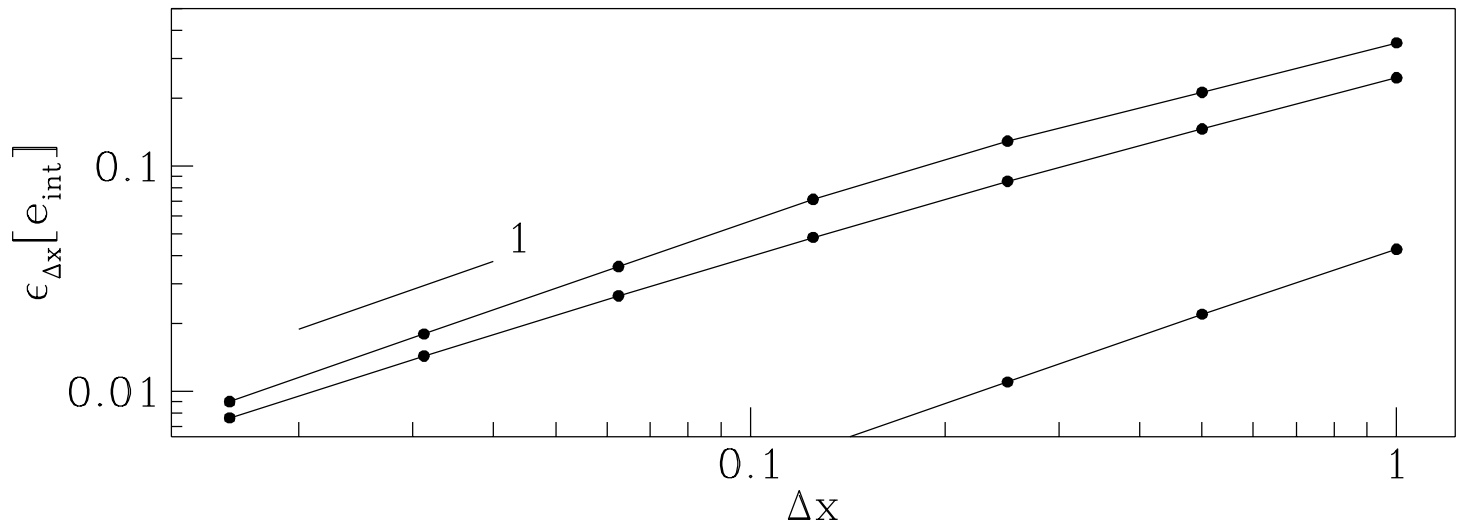
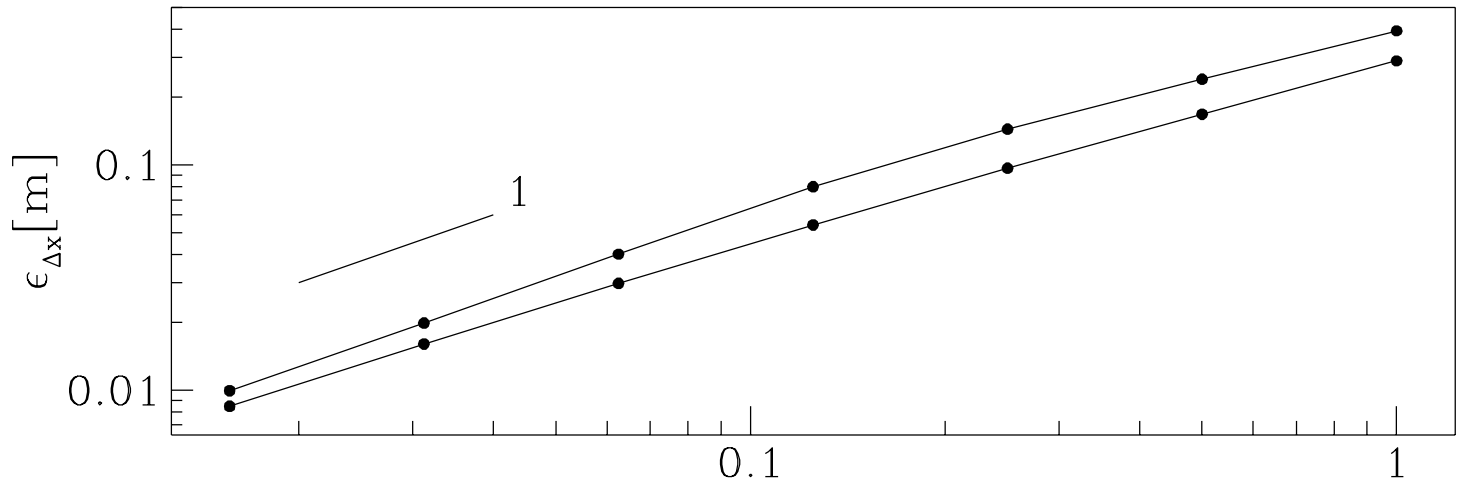
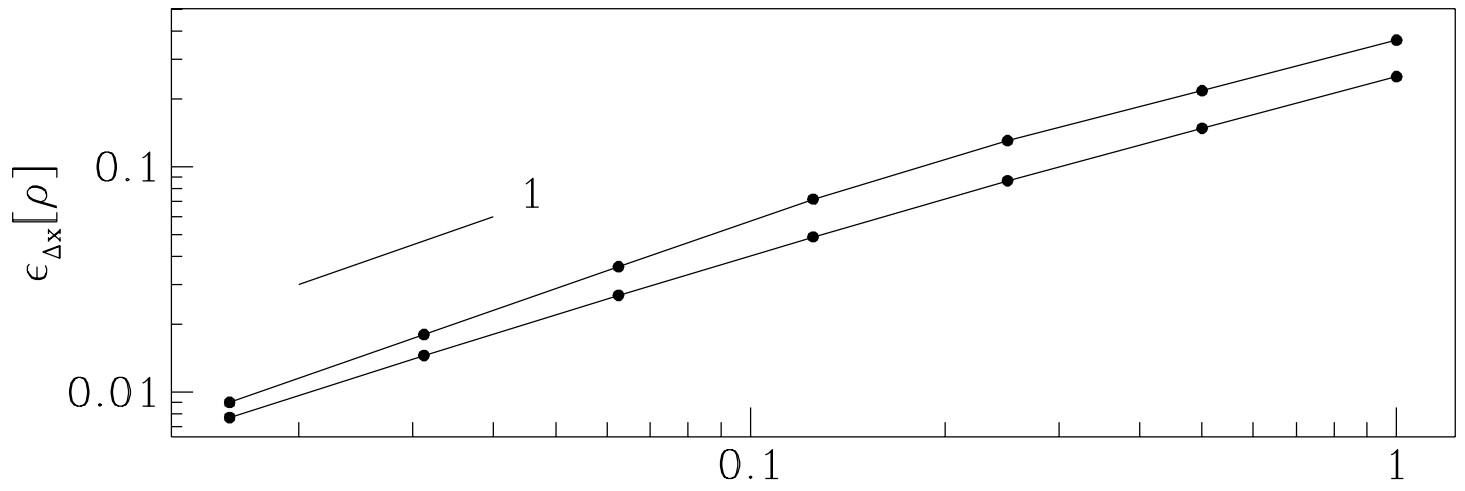


This figure "fig1-2.png" is available in "png" format from:

<http://arxiv.org/ps/astro-ph/9311019v1>

This figure "fig2-2.png" is available in "png" format from:

<http://arxiv.org/ps/astro-ph/9311019v1>

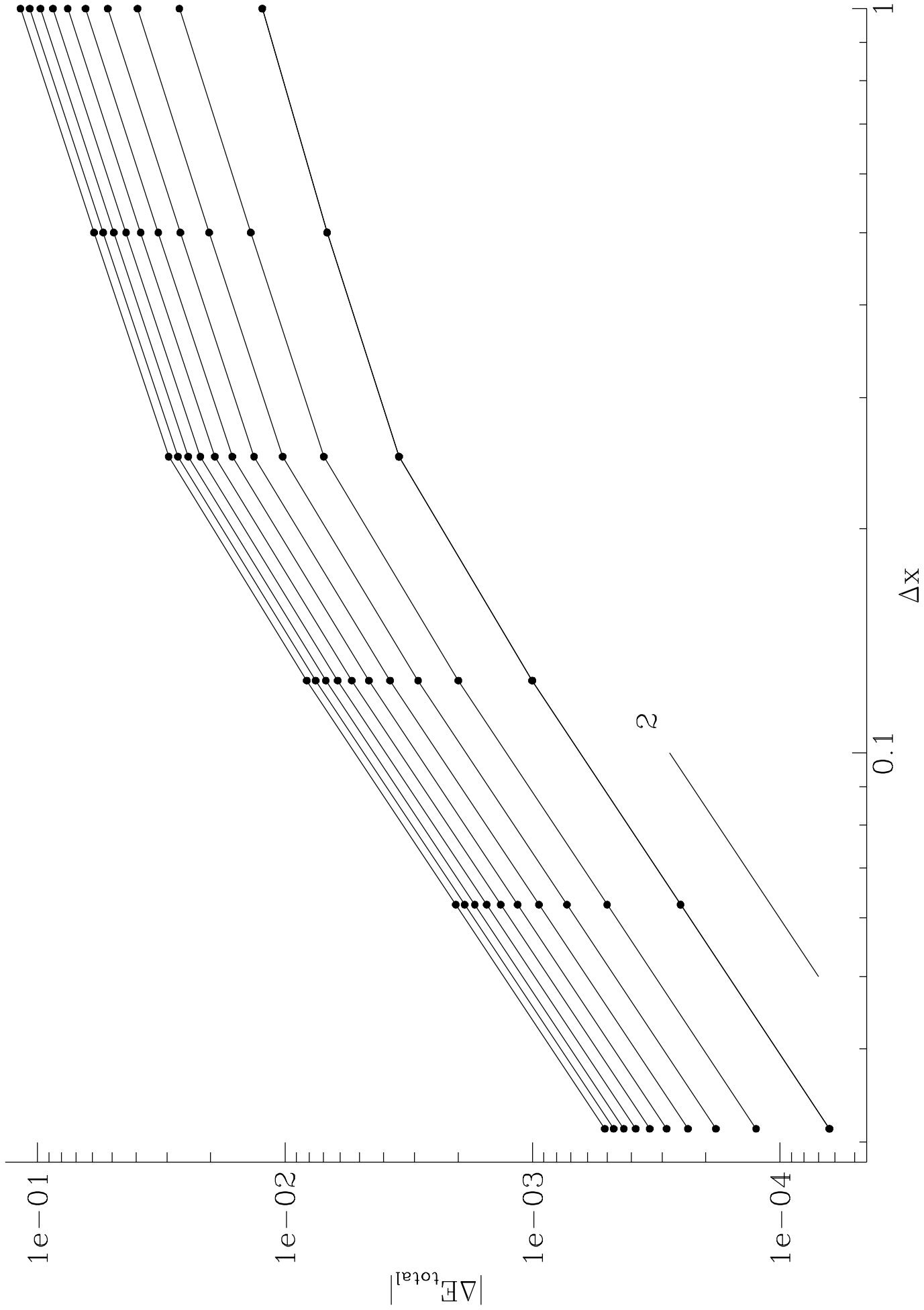


This figure "fig1-3.png" is available in "png" format from:

<http://arxiv.org/ps/astro-ph/9311019v1>

This figure "fig2-3.png" is available in "png" format from:

<http://arxiv.org/ps/astro-ph/9311019v1>

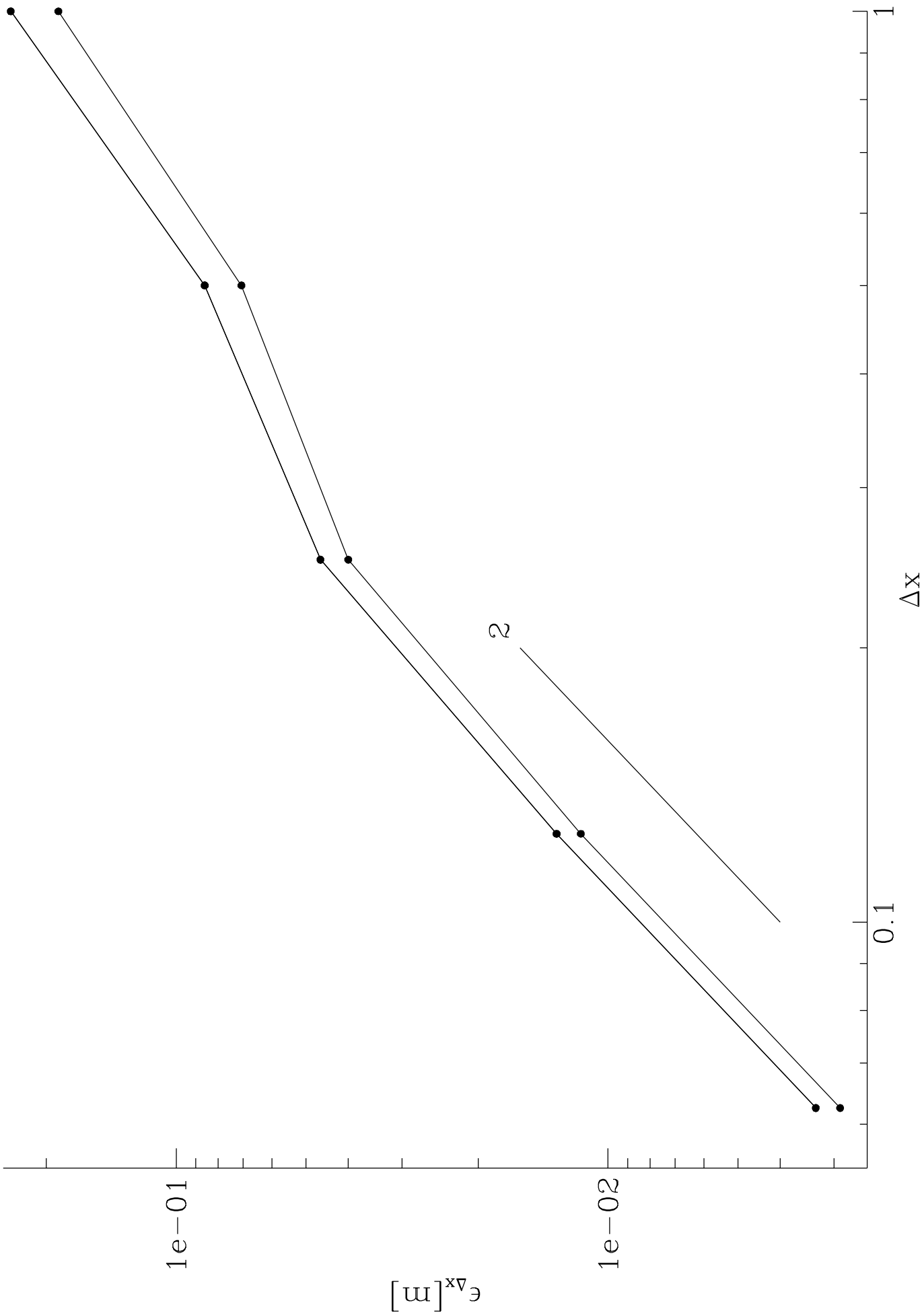


This figure "fig1-4.png" is available in "png" format from:

<http://arxiv.org/ps/astro-ph/9311019v1>

This figure "fig2-4.png" is available in "png" format from:

<http://arxiv.org/ps/astro-ph/9311019v1>

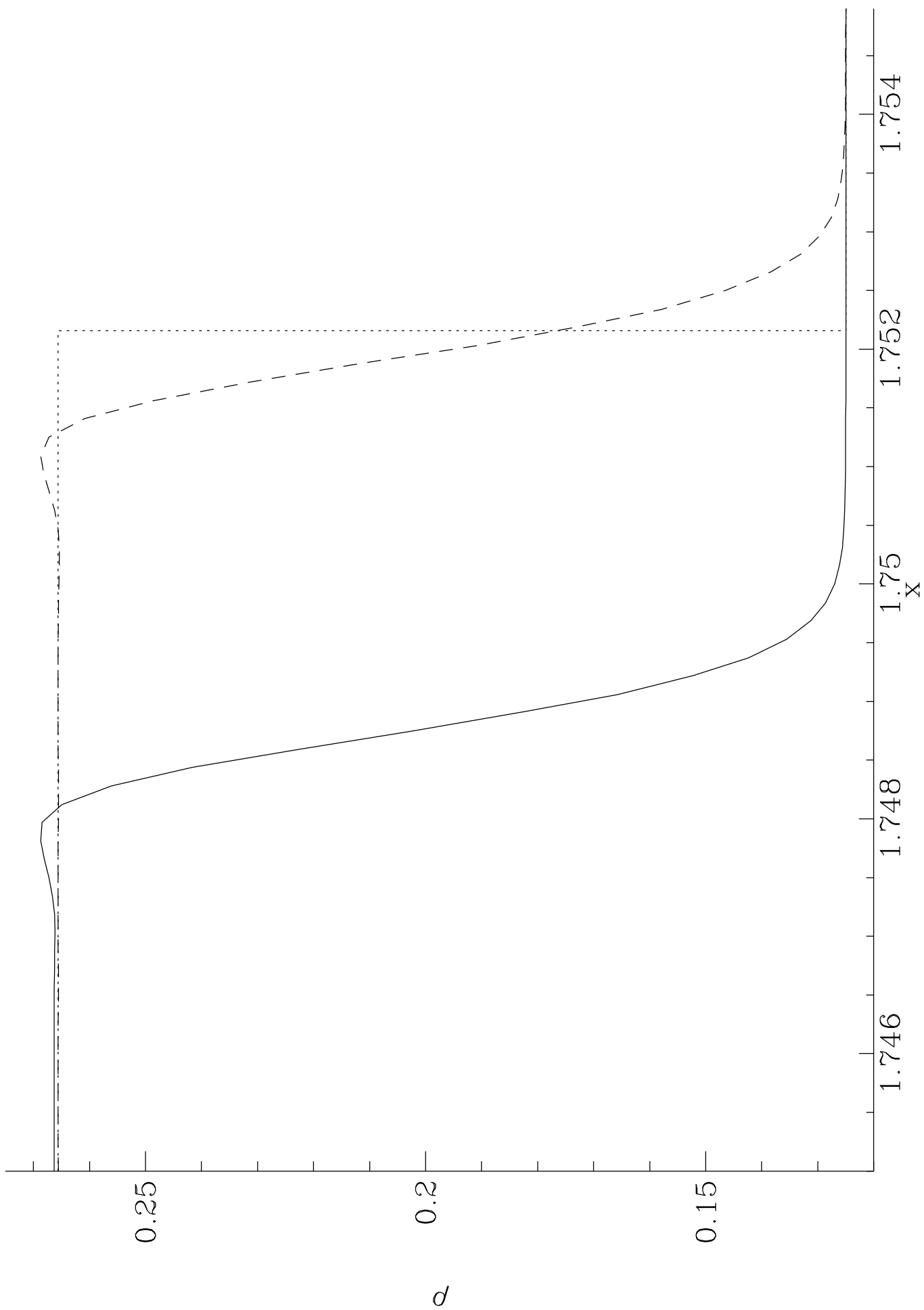


This figure "fig1-5.png" is available in "png" format from:

<http://arxiv.org/ps/astro-ph/9311019v1>

This figure "fig2-5.png" is available in "png" format from:

<http://arxiv.org/ps/astro-ph/9311019v1>

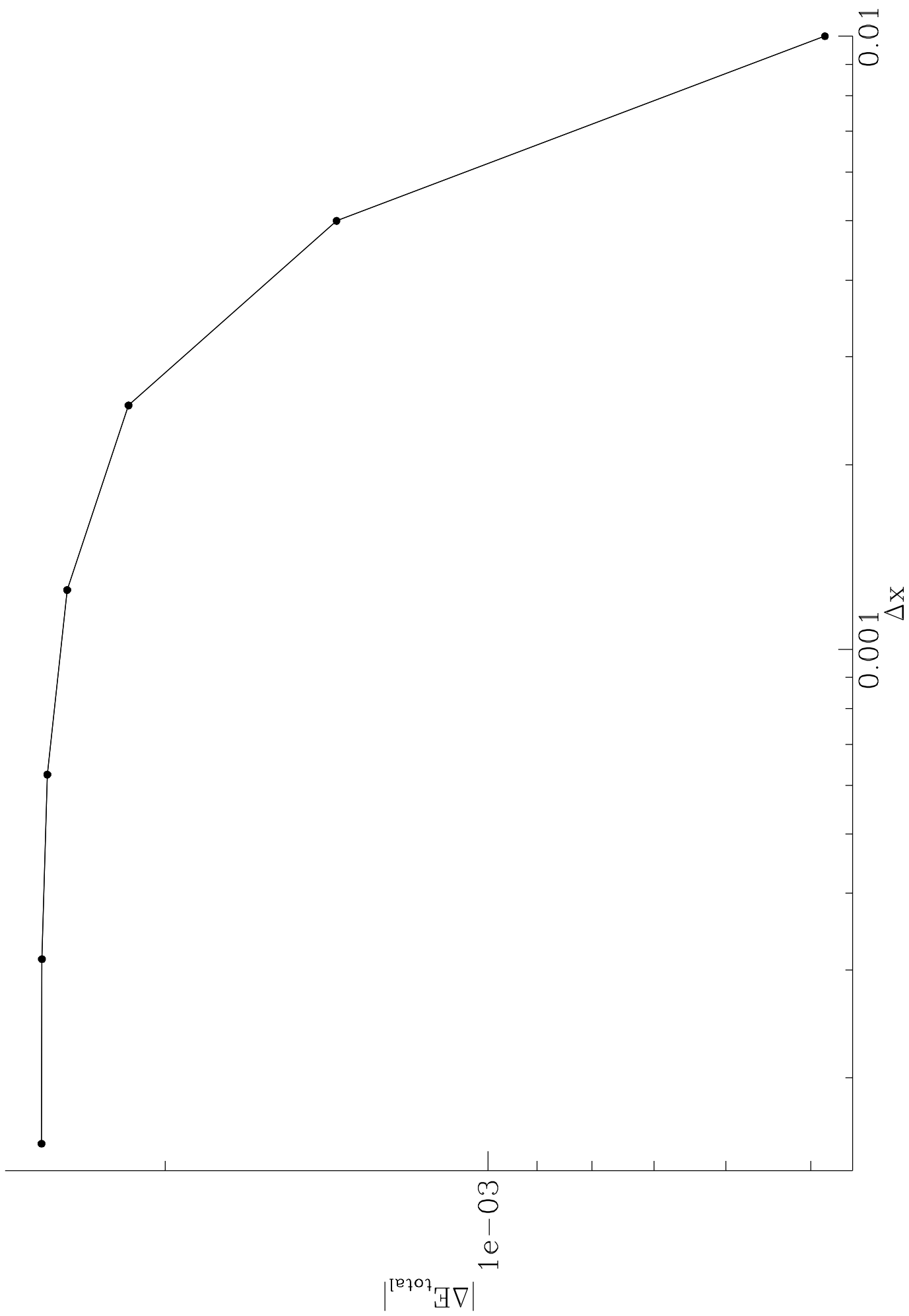


This figure "fig1-6.png" is available in "png" format from:

<http://arxiv.org/ps/astro-ph/9311019v1>

This figure "fig2-6.png" is available in "png" format from:

<http://arxiv.org/ps/astro-ph/9311019v1>

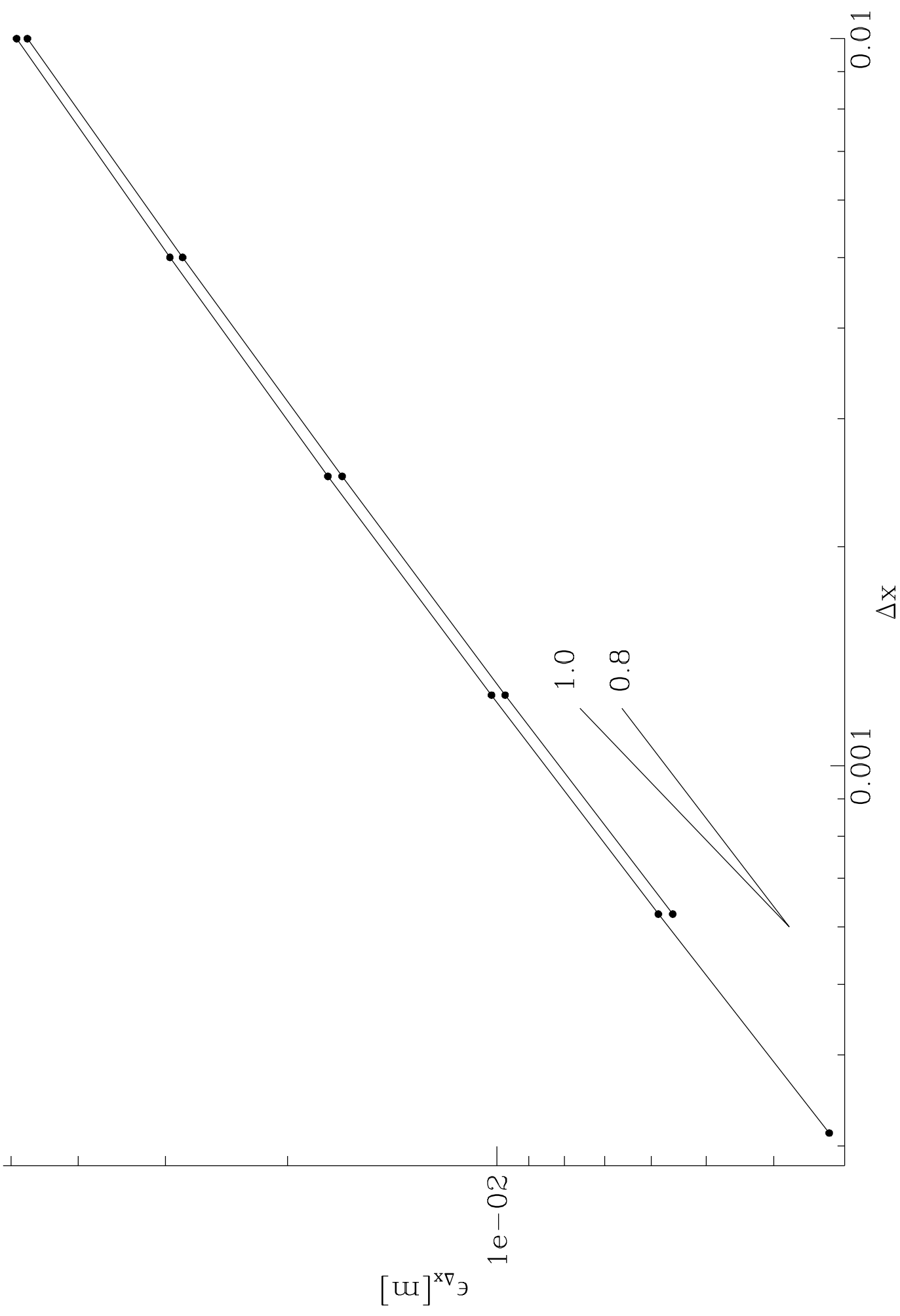


This figure "fig1-7.png" is available in "png" format from:

<http://arxiv.org/ps/astro-ph/9311019v1>

This figure "fig2-7.png" is available in "png" format from:

<http://arxiv.org/ps/astro-ph/9311019v1>

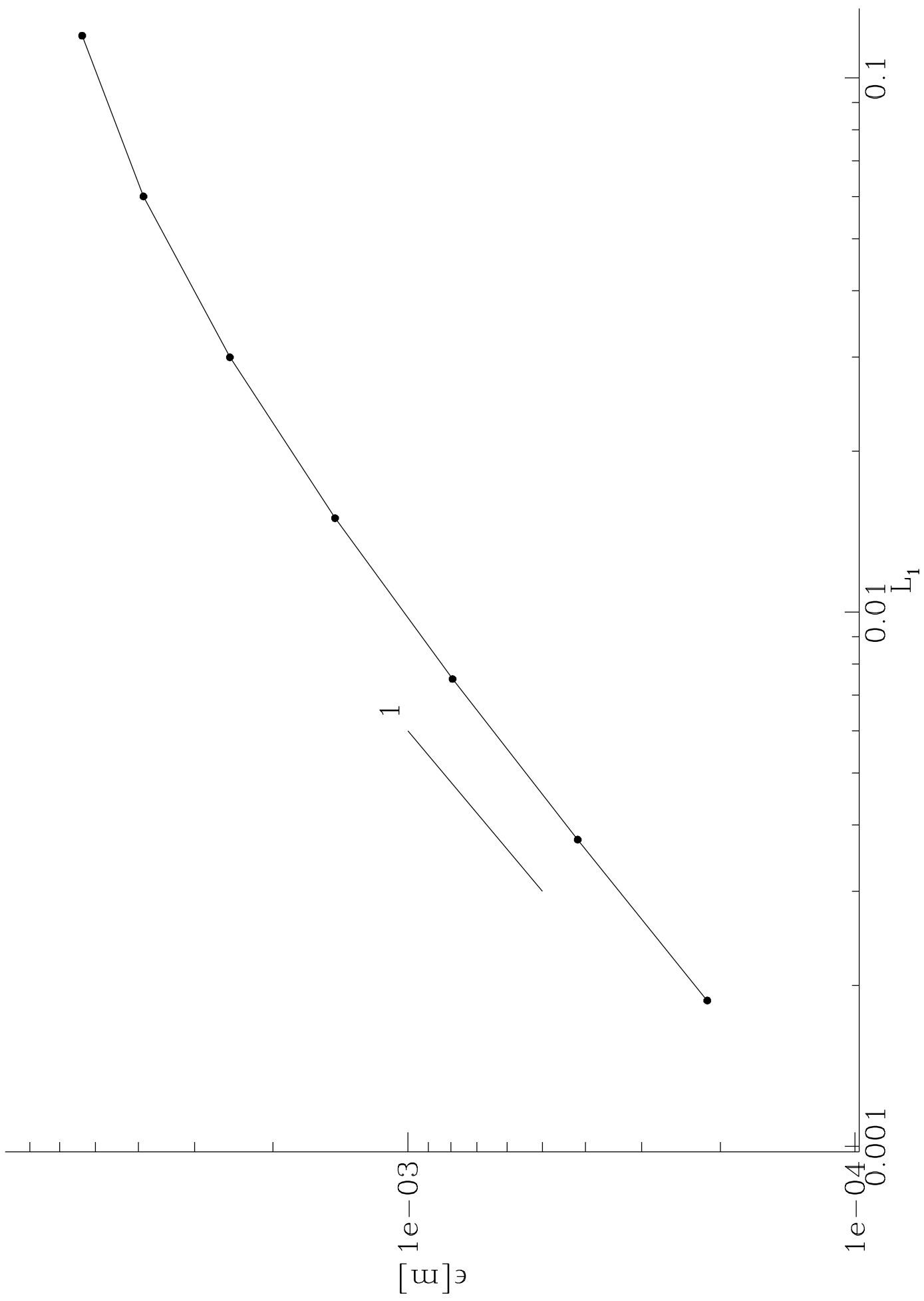


This figure "fig1-8.png" is available in "png" format from:

<http://arxiv.org/ps/astro-ph/9311019v1>

This figure "fig2-8.png" is available in "png" format from:

<http://arxiv.org/ps/astro-ph/9311019v1>

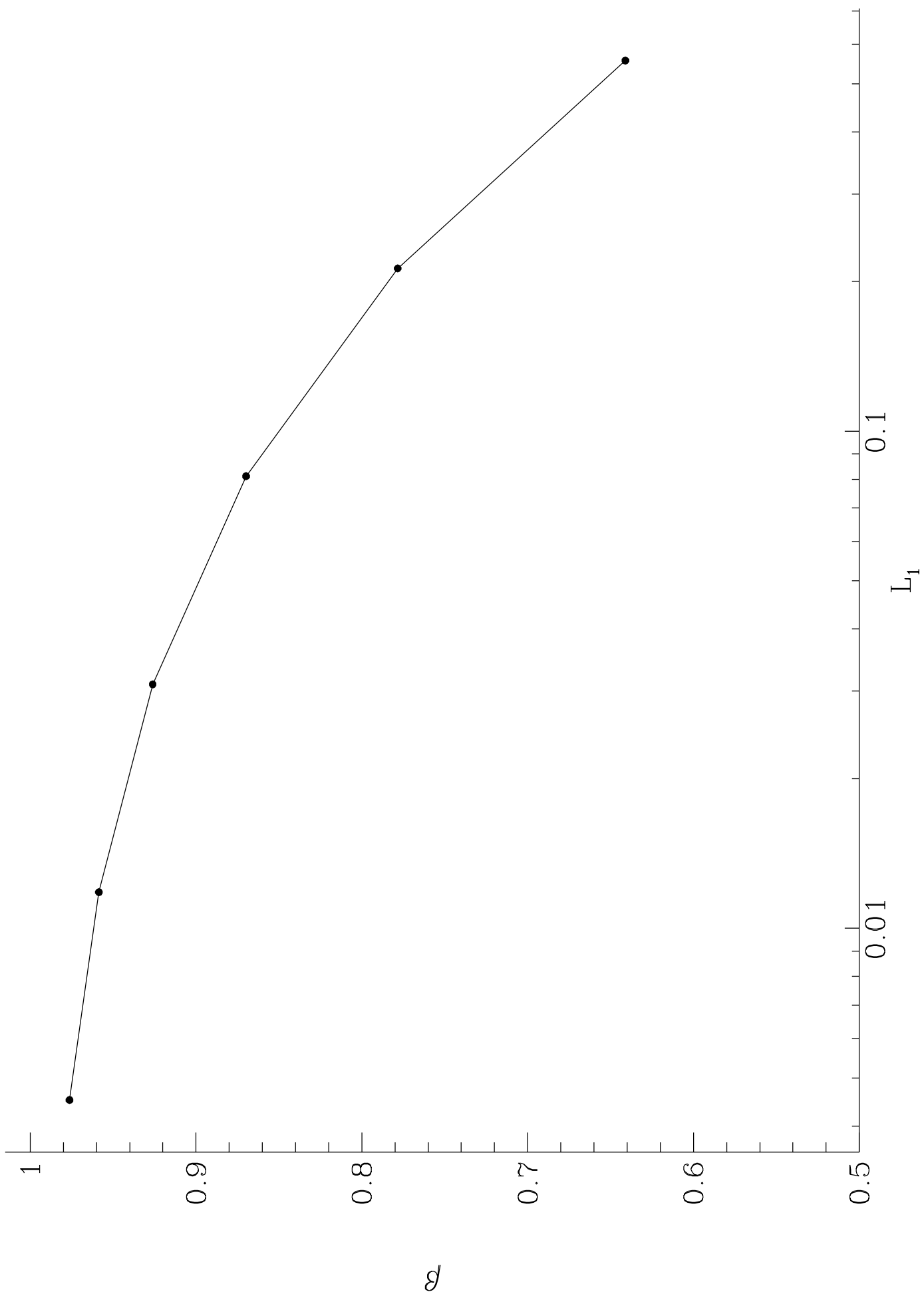


This figure "fig1-9.png" is available in "png" format from:

<http://arxiv.org/ps/astro-ph/9311019v1>

This figure "fig2-9.png" is available in "png" format from:

<http://arxiv.org/ps/astro-ph/9311019v1>

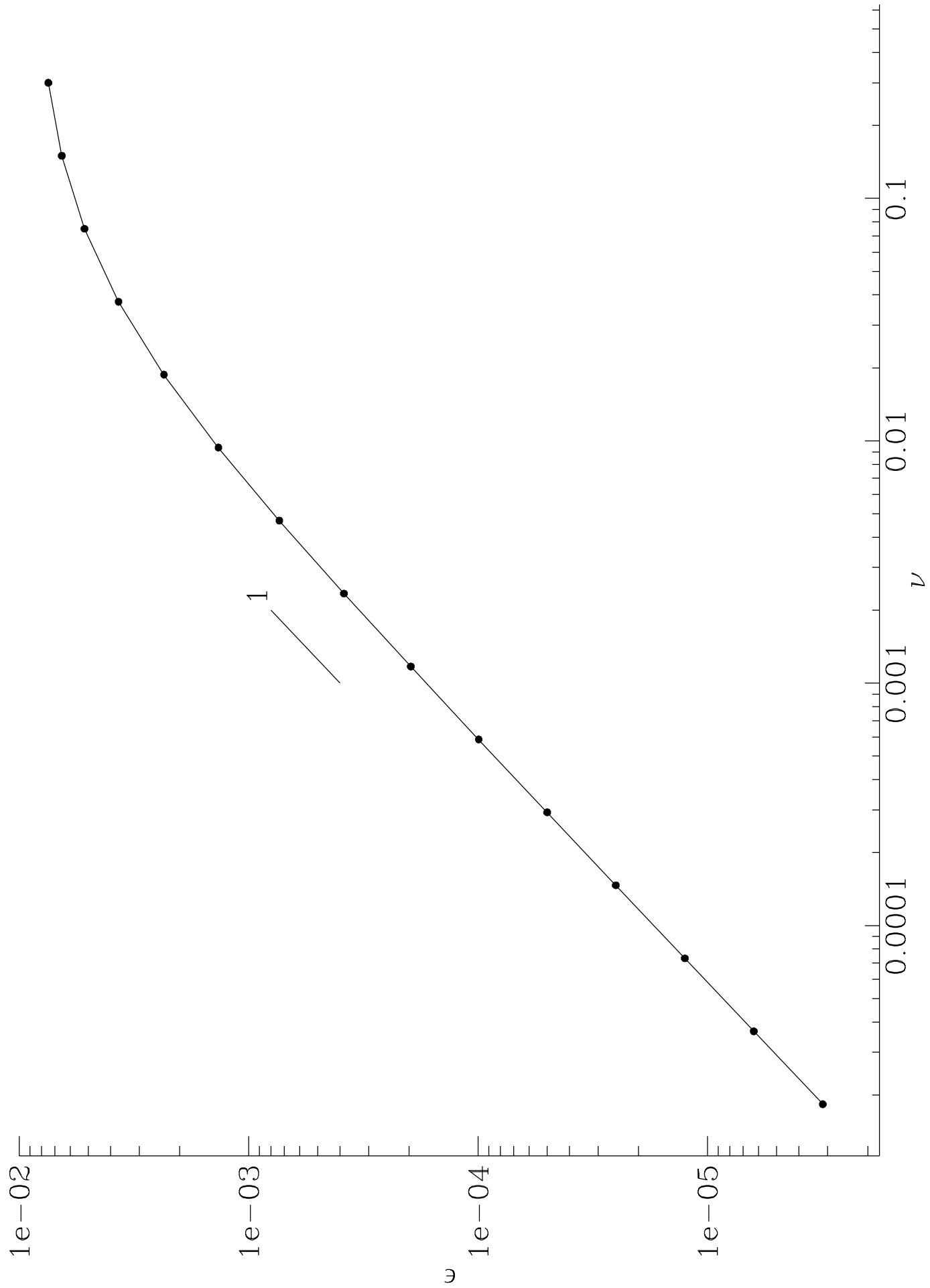


This figure "fig1-10.png" is available in "png" format from:

<http://arxiv.org/ps/astro-ph/9311019v1>

This figure "fig2-10.png" is available in "png" format from:

<http://arxiv.org/ps/astro-ph/9311019v1>



This figure "fig1-11.png" is available in "png" format from:

<http://arxiv.org/ps/astro-ph/9311019v1>

